

# [O III] $\lambda 5007$ emissions in extremely red quasars (ERQs) are compact

Marie Wingyee Lau,<sup>1\*</sup> Serena Perrotta,<sup>2</sup> Fred Hamann,<sup>1</sup> Jarred Gillette,<sup>1,3</sup>  
David S. N. Rupke,<sup>4,5</sup> Andrey Vayner,<sup>6</sup> Nadia L. Zakamska<sup>6</sup> Dominika Wylezalek<sup>5</sup>

<sup>1</sup>Department of Physics & Astronomy, University of California, Riverside, CA 92521, USA

<sup>2</sup>Center for Astrophysics and Space Sciences, University of California, San Diego, CA 92093, USA

<sup>3</sup>Eureka Scientific, Oakland, CA 94602, USA

<sup>4</sup>Department of Physics, Rhodes College, Memphis, TN 38112, USA

<sup>5</sup>Astronomisches Rechen-Institut, Zentrum für Astronomie der Universität Heidelberg, D-69120 Heidelberg, Germany

<sup>6</sup>Department of Physics & Astronomy, Johns Hopkins University, Baltimore, MD 21218, USA

Accepted XXX. Received YYY; in original form ZZZ

## ABSTRACT

“Extremely red quasars” (ERQs) are a non-radio-selected, intrinsically luminous population of quasars at cosmic noon selected by their extremely red colour from rest-frame UV to mid-IR. ERQs are uniquely associated with exceptionally broad and blueshifted [O III]  $\lambda 5007$  emission reaching speeds  $>6000 \text{ km s}^{-1}$ . We obtained adaptive optics integral-field spectroscopic observations using Keck/OSIRIS and Gemini/NIFS of a sample of 10 ERQs with bolometric luminosities ( $10^{47.0}–10^{47.9}$ )  $\text{erg s}^{-1}$  at  $z \sim (2.3–3.0)$ . The goal is to measure the sizes and spatially-resolved kinematics of the [O III]-emitting regions. We study the surface brightness maps and aperture-extracted spectra and model the point-spread functions. We identify signs of merger activities in the continuum emissions. We identify physically distinct [O III] kinematic components that are bimodal and respectively trace ERQ-driven outflows of velocity dispersion  $\geq 250 \text{ km s}^{-1}$  and dynamically quiescent interstellar media. We find that the ERQ-driven ionized outflows are typically at  $\sim 1 \text{ kpc}$  scales whereas the quiescent ionized gas extend to a few kpc. Compared to normal quasars the extremely fast ERQ-driven [O III] outflows tend to be more compact, supporting the notion that ERQs are in a young stage of quasar/galaxy evolution and represent unique physical conditions beyond orientation differences with normal quasar populations. The kinematically quiescent [O III] emissions in ERQs tend to be spatially-resolved but less extended than in normal quasars, which can be explained by global and patchy dust obscuration. The hint of ionization cones suggests some of the obscuration can be partially explained by a patchy torus.

**Key words:** quasars: emission lines – quasars: general – galaxies: kinematics and dynamics – galaxies: active – galaxies: evolution – galaxies: high-redshift

## 1 INTRODUCTION

Quasar outflows have been invoked in galaxy evolution models to regulate or halt both star formation in their host galaxies and the accretion of material onto the central supermassive black holes. In certain theoretical scenarios, after triggering events for massive starbursts that shroud the galaxies in gas and dust, important feedback of quasar outflows is expected to occur during a brief dusty “blowout” phase of galaxy evolution. During this particular “blowout” stage outflows remove dust and gas from their hosts, revealing the visibly luminous quasars and driving the transition from the initial dusty starbursts to the later quiescent galaxy phases (e.g. Sanders et al. 1988; Hopkins et al. 2006, 2008, 2016) Feedback from quasar outflows can also aide in establishing the black hole–bulge correlations in the local universe (Gebhardt et al. 2000; Hopkins et al. 2006), and prevent the overgrowth of massive galaxies (Croton et al. 2006).

Adaptive-optics-assisted and spaceborne integral-field spectroscopy have established that ionized outflows driven by radio-loud or jetted sources, as well as the much more common radio-quiet quasars, can have a major impact on the gas reservoir in their host galaxies especially at high redshifts (e.g. Cresci et al. 2015; Perna et al. 2015; Brusa et al. 2016; Nesvadba et al. 2017; Williams et al. 2017; Kakkad et al. 2020; Perna et al. 2023; Vayner et al. 2021b; Cresci et al. 2023; Veilleux et al. 2023). However, the impact of ionized outflows from obscured, dust-reddened radio-quiet quasars on their host galaxies has only recently begun to be explored with high-resolution integral-field data. Radiation-hydrodynamic simulations predict that reprocessing quasar radiation and trapping the IR radiation by dust can launch fast galactic outflows (Costa et al. 2018; Soliman & Hopkins 2023).

Detailed observational studies at high redshift are challenging due to a combination of dust reddening and cosmic surface brightness dimming (see e.g. Perna et al. 2015; Chen et al. 2017). Obscured, dust-reddened quasars are particularly important for studies of quasar feedback because they are believed to be still partially embedded in

\* E-mail: wingyeel@ucr.edu (MWL)

dusty starbursts (e.g. Canalizo & Stockton 2001; Urrutia et al. 2008; Assef et al. 2015; Banerji et al. 2015; Noboriguchi et al. 2019; Calistro Rivera et al. 2021; Glikman et al. 2022). Obscured quasars are therefore prime candidates for quasars actively clearing their hosts and disrupting star formation. The [O III]  $\lambda 5007$  emission line, being a low density-forbidden transition, is particularly important for identifying outflows on galactic, kpc scales. At lower redshifts  $z \sim 0.5$ , past integral-field observations of the [O III]  $\lambda 5007$  emission in radio-quiet obscured quasars found outflow signatures of velocities  $\sim 800 \text{ km s}^{-1}$  in essentially all targets examined (Liu et al. 2013; Shen et al. 2023). These observations demonstrate that ionized outflows in radio-quiet quasars are powerful and ubiquitous.

However, it is at the peak epoch of galaxy formation and quasar activity,  $z \sim 2-3$ , that quasar feedback should have the greatest impact on massive galaxy evolution. Recently, a remarkable population of “extremely red quasars” (ERQs) at  $z \sim 2-3$  have been discovered in the Sloan Digital Sky Survey-III Baryon Oscillation Sky Survey (BOSS; Ross et al. 2015; Hamann et al. 2017). ERQs have extremely red colours in the rest-frame UV to mid-IR, high bolometric luminosities  $> 10^{47} \text{ erg s}^{-1}$ , normal to quiet radio luminosities  $\sim 10^{41} \text{ erg s}^{-1}$ , and sky densities a few per cent of luminous blue quasars consistent with being a short obscured phase of quasar activity. ERQs might also be cosmic-noon analogs of “extremely red objects” (EROs, likely to be quasars) discovered recently at  $z \sim 5-9$  with JWST (Barro et al. 2023; Noboriguchi et al. 2023). Importantly, ERQs also have a suite of extreme spectral properties unlike any other known quasar populations (Monadi & Bird 2022; Gillette et al. 2024). Near-IR longslit spectroscopy revealed that ERQs systematically have among the broadest and most blueshifted [O III]  $\lambda 5007$  lines ever reported with FWHM velocities and blueshifted wings reaching  $> 6000 \text{ km s}^{-1}$  (Zakamska et al. 2016; Perrotta et al. 2019). Such extreme [O III] outflows have only been observed in one other population called the hot dust-obscured galaxies (Hot DOGs) which overlap with the ERQ population (Finnerty et al. 2020). These velocities are too large to be contained by any realistic galaxy potential and are tell-tale signs of powerful outflows. These extreme [O III] outflows are strongly correlated with the extreme red colours of ERQs, and not with radio loudness, high bolometric luminosities, or high Eddington ratios (Shen 2016; Bischetti et al. 2017). The [O III] outflows from ERQs are typically three times faster than in blue quasars at similar redshifts and luminosities. Perrotta et al. (2019) also estimated that the [O III] outflows from ERQs have kinetic energy luminosities at a few per cents of the quasar bolometric luminosities, which should be sufficient to drive important feedback in the host galaxies (e.g. Hopkins & Elvis 2010; Zubovas & King 2012).

Lau et al. (2022) and Gillette et al. (2023) observed the Ly $\alpha$ -emitting haloes around ERQs and found they are kinematically quiet down to the spatial resolution  $\sim 6 \text{ kpc}$  from the central quasars. This implies that the spatial scales of the extremely fast outflows extend out to less than  $\sim 6 \text{ kpc}$ , although this does not rule out the presence of an undetected underdense phase of fast circumgalactic-scale outflows (Nelson et al. 2019; Costa et al. 2022). With spaceborne or adaptive-optics integral-field observations we can directly measure the extents of the [O III]  $\lambda 5007$  outflows on galactic scales. Detailed study of one ERQ using the Near Infrared Spectrograph (NIRSpec) onboard JWST and the Near-Infrared Integral Field Spectrograph (NIFS) on the Gemini North telescope (Gemini-N) has been published (Vayner et al. 2021a; Wylezalek et al. 2022; Vayner et al. 2023, 2024). Its [O III] emission traces powerful, extensive outflows out to 10 kpc and clumpy ionized gas in the host out to at least 16 kpc.

To determine the characteristic sizes and the spatially resolved kinematics of the [O III] emissions in ERQs as a population, we car-

ried out adaptive-optics observations of nine more ERQs using the OH-Suppressing Infrared Integral Field Spectrograph (OSIRIS) on the Keck I telescope, forming a total sample of 10. In this paper we test the hypothesis that ERQs are generally young objects whose high-speed ionized outflows have not had time to further expand into their host interstellar media. In addition to statistically characterizing the extents of the [O III]-traced outflows, we also measure the extents of the more quiescent [O III]-traced interstellar media whenever detected. These measurements of the [O III]-traced interstellar media complement the measurements of continuum-traced starlight in Zakamska et al. (2019). In this work we do not attempt to quantitatively assess dust extinction due to the large systematic uncertainties involved.

This paper is organized as follows. Section 2 describes the observations and data reduction. Section 3 describes the data analysis procedures and the results. Section 4 discusses the implications of our findings in the context of other quasars in the literature. Section 5 presents the conclusions. Throughout this paper we adopt a  $\Lambda$  cold dark matter cosmology with  $H_0 = 69.6 \text{ km s}^{-1} \text{ Mpc}^{-1}$ ,  $\Omega_M = 0.286$ ,  $\Omega_\Lambda = 0.714$ , as adopted by the online cosmology calculator developed by (Wright 2006) at the time of this writing. All distances are proper. For the redshift range covered by this sample 2.3–3.0, 1 arcsec corresponds to (8.4–7.9) kpc. We use photometric magnitudes in the AB system. We report vacuum wavelengths in the heliocentric frame and name the line transitions by their air wavelengths.

## 2 OBSERVATIONS AND DATA REDUCTION

### 2.1 Sample Selection

We select targets with existing longslit [O III] spectra from Perrotta et al. (2019), with a preference for sources with very red colours and/or very fast [O III] outflows. The only exception is J2223+0857, for which we present the first [O III] observations here. Table 1 lists some previously-reported basic properties of the ERQs in this sample. The “extremely-red” colour is defined by  $i - W3 > 4.6$  from the Sloan Digital Sky Survey-III (Eisenstein et al. 2011) and the Wide-field Infrared Survey Explorer (Wright et al. 2010). For reference, the  $i - W3$  colours of this work range between (3.8–8.0) while that of Perrotta et al. (2019) range between (3.3–8.0). The [O III]  $\lambda 5007 w_{90}$  velocity widths (defined as encompassing 90% of the line fluxes) of this work and Perrotta et al. (2019) both range between (2450–7230)  $\text{km s}^{-1}$ . Sources of this sample are classified as ERQs except J1550+0806, which is listed as a red “ERQ-like” quasar by Hamann et al. (2017) based on extreme emission-line properties like ERQs but with a less extreme red  $i - W3$  colour. J1550+0806 has  $i - W3 = 3.8$  which is still significantly redder the median of  $W3$ -detected BOSS quasars at  $i - W3 = 2.5$ . This red ERQ-like quasar overlaps with ERQs in many emission-line properties including high rest equivalent widths and extreme [O III] kinematics, and its measurements does not skew any results on the ERQ sample. Figure 1 shows the  $i - W3$  distributions of this sample and the Perrotta et al. (2019) sample. For simplicity we refer to all our targets as ERQs. When available, we obtain accurate systemic redshifts measured from CO host emission, Ly $\alpha$  halo emission, or “spike”-like narrow Ly $\alpha$  quasar emission as reported in Gillette et al. (2024). The intrinsic bolometric luminosities are estimated from applying a bolometric correction factor of 8 to the rest-frame  $5 \mu\text{m}$  luminosities extrapolated from the  $W3$ -band photometry.

We choose to target the [O III]  $\lambda\lambda 4959, 5007$  emissions over the H $\alpha$  emissions. The H $\alpha$ -traced outflow and interstellar medium emissions

are difficult to extract as they are heavily blended with the broad-line region and [N II]  $\lambda\lambda 6549, 6584$  emissions (see Vayner et al. 2021a; Kakkad et al. 2023). This sample is a total of 10 ERQs observed with laser-guided adaptive-optics-assisted near-IR integral-field spectrographs. We include ERQ J1652+1728 which has Gemini-N/NIFS observations and good adaptive optics correction published in Vayner et al. (2021a). One more ERQ J2323–0100 has shallower Keck-I/OSIRIS observations briefly described in Vayner et al. (2021a). We obtained deeper OSIRIS observations of this source plus new observations of other ERQs.

We select targets based on availability of nearby bright stars, existence of multiwavelength data, observation scheduling constraints due to object visibility, object brightness, and weather conditions. To enable tip/tilt correction by the Keck I laser guide star adaptive optics system, we require availability of an  $r < 17$  mag star within  $\sim 50$  arcsec of the science target. All but one ERQ, J2223+0857, in this sample have existing near IR longslit spectra where [O III] kinematics and energetics are already analyzed (Perrotta et al. 2019), and six of them have Atacama Large Millimeter Array Band 6 observations for measuring molecular gas and dust (F. Hamann et al., in preparation). The long requisite exposure times and complex mechanics of the laser guide star adaptive optics system limit observation scheduling to at most one target per half good night.

## 2.2 Observing and Reducing Data

The published NIFS observations of J1652+1728 has a wavelength range of the full  $K$ -band and a field of view of  $3 \times 3$  arcsec<sup>2</sup>, and has an absolute flux uncertainty at 10–15 per cent. OSIRIS provides spectroscopy with median resolution  $R \sim 3800$  with a variable field-of-view utilizing a lenslet design. The OSIRIS observations were conducted in the Hn3, Hn4, and Hn5 narrowband filters using the 50 milliarcsec plate scale mode. The Hn3 filter allows extracting a wavelength range of (15940–16760) Å and a field of view of  $2.4 \times 3.2$  arcsec<sup>2</sup> per frame. The Hn4 filter has a wavelength range of (16520–17370) Å and a field of view of  $2.1 \times 3.2$  arcsec<sup>2</sup>. The Hn5 filter has a wavelength range of (17210–1808) Å and a field of view of  $1.6 \times 3.2$  arcsec<sup>2</sup>. We observed the tip/tilt stars immediately before and in between their science target frames. During science exposures we dithered along the short axis to enlarge the field of view, yielding a final co-added field-of-view ranging from  $1.7 \times 2.4$  arcsec<sup>2</sup> to  $2.8 \times 2.8$  arcsec<sup>2</sup> with the edges trimmed. The chosen field of view was informed by the extent of the [O III] emission in the NIFS observations of J1652+1728. To enable sky subtraction we nodded by 5 arcsec from the science target to blank sky in the repeating object-sky-object sequences. The exposure time of each frame was 900 s and the total on-source exposure times ranged from 2700 s to 18000 s. To correct for atmospheric absorption and to flux calibrate the final co-added science cube, telluric standard stars were observed with the same setup as the science observations within 0.2 airmass of the average of the science observations before or after the science observations. Spectral types of the standard stars are close to A0. In Table 2 we present the logs of the OSIRIS observations. The reference adaptive-optics-corrected point spread function (PSF) sizes are measured from fitting Gaussian models to the azimuthally-averaged surface brightness radial profiles of the paired tip/tilt stars or the H $\beta$  broad line region of the ERQs, which range from 0.15 arcsec to 0.23 arcsec.

For each science target, we reduced the OSIRIS observations using the Keck OSIRIS Spectroscopic Data Reduction Pipeline (Lyke et al. 2017; Lockhart et al. 2019) and the general-purpose IDL library ISFRED (Rupke 2014). The OSIRIS pipeline first creates a master

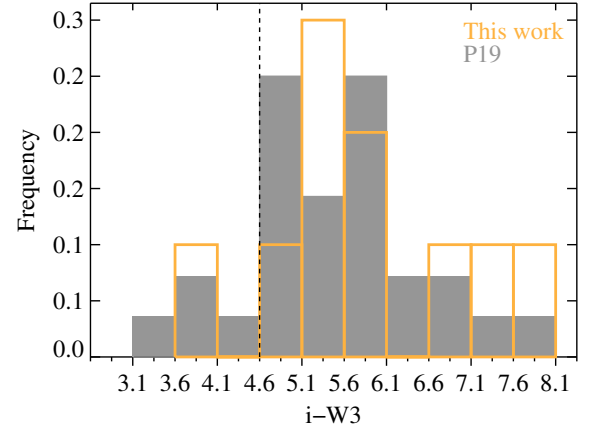


**Figure 1.** Histograms of the  $i - W3$  colours of the ERQs and ERQ-like sources in this integral-field sample and the Perrotta et al. (2019) longslit sample. The dotted line marks the ERQ definition of  $i - W3 > 4.6$ .

dark by median-combining several dark observations taken in the afternoon. After dark subtraction, the OSIRIS pipeline extracts the spectra using a Lucy-Richardson deconvolution using a known point spread function for each lenslet stored in the rectification matrix. The OSIRIS pipeline then applies wavelength calibration and combines the spectra into a three-dimensional data cube. The OSIRIS pipeline performs scaled sky subtraction by scaling families of OH emission lines in the sky cubes to match the science observations. The OSIRIS pipeline then removes the telluric absorption features by removing hydrogen features from the telluric star spectrum, dividing by a blackbody, normalizing it, and then dividing this response function into the science frames. Using routines of the IFSRED library we performed further sky subtraction by selecting a sky aperture in each science frame and subtracting the spatial median of it across the entire field. We aligned the individual reduced data cubes using the position of the quasar centroid and median-combined them. We extracted the standard star flux and compared to existing  $H$ -band photometry to obtain the absolute flux per unit count per second, and absolute-flux-calibrated the mosaicked science data cube. We estimate the absolute fluxing accuracy at 10–15 per cent. Finally we visually examined the reduced, mosaicked, flux-calibrated science data cube for any unaccounted background artifacts caused by the complex optics and manually subtracted them.

## 3 ANALYSIS AND RESULTS

As the spatially-integrated [O III] kinematics have been analyzed in Perrotta et al. (2019), this work focuses on the spatial extents and the spatially resolved kinematics. Due to limited signal-to-noise (S/N) we do not attempt to examine the spectra spaxel by spaxel, but rather we examine narrowband images and aperture spectra. We first create narrowband continuum and [O III] images and spatially-integrated spectra for quicklook visualization of the adaptive optics data. Then we use two techniques, namely the radial profile method and the PSF subtraction method, to carefully assess if the continuum and [O III] emissions are extended. We consider emission to be extended if either technique reveals it to be extended. After that we assess the

**Table 1.** Basic Properties of ERQs Observed with Adaptive Optics

Name	R.A.	Dec.	Systemic Redshift (Indicator) <sup>a</sup>	$i-W3^b$	Bolometric Luminosity ( $\text{erg s}^{-1}$ ) <sup>c</sup>
J0006+1215	00:06:10.67	+12:15:01.2	2.3183 (CO)	8.0	$7.58 \times 10^{47}$
J0209+3122	02:09:32.15	+31:22:02.7	2.3595 ( $H\beta$ )	5.1	$1.02 \times 10^{47}$
J1031+2903	10:31:46.53	+29:03:24.1	2.2956 ([O III])	6.0	$1.91 \times 10^{47}$
J1217+0234	12:17:04.70	+02:34:17.1	2.4280 (CO)	5.7	$2.49 \times 10^{47}$
J1232+0912	12:32:41.73	+09:12:09.3	2.4050 (CO)	5.6	$6.34 \times 10^{47}$
J1550+0806	15:50:57.71	+08:06:52.1	2.5088 ( $H\beta$ )	6.8	$1.16 \times 10^{47}$
J1604+5633	16:04:31.55	+56:33:54.2	2.4914 (Low ions)	3.8	$1.96 \times 10^{47}$
J1652+1728	16:52:02.64	+17:28:52.3	2.9548 ( $Ly\alpha$ halo)	5.7	$6.80 \times 10^{47}$
J2223+0857	22:23:07.12	+08:57:01.7	2.2902 (CO)	5.4	$1.73 \times 10^{47}$
J2323-0100	23:23:26.17	-01:00:33.1	2.3805 (CO)	5.6	$2.87 \times 10^{47}$

<sup>a</sup>Obtained from Perrotta et al. (2019) and Gillette et al. (2024).

<sup>b</sup>Obtained from SDSS and WISE photometry.

<sup>c</sup>Estimated based on  $W3$ -band photometry.

**Table 2.** Observing Logs of ERQs

Name	Date (UT)	Instrument	Band ( $\text{\AA}$ )	Field of View <sup>a</sup> (arcsec $\times$ arcsec)	Integration Time (s)	Airmass	Seeing (arcsec)	Corrected PSF (Indicator) <sup>b</sup> (arcsec/kpc)
J0006+1215	2020 Oct 3	OSIRIS	Hn3/(15940–16760)	2.8 $\times$ 2.8	8100	1.1	0.9	0.17/1.4 (tip/tilt star)
J0209+3122	2020 Oct 3	OSIRIS	Hn4/(16520–17370)	2.8 $\times$ 2.8	9000	1.1	0.9	0.19/1.6 (tip/tilt star)
J1031+2903	2021 May 3	OSIRIS	Hn3/(15940–16760)	2.4 $\times$ 2.8	2700	1.1	0.7	0.19/1.6 (tip/tilt star)
J1217+0234	2021 May 4	OSIRIS	Hn4/(16520–17370)	2.4 $\times$ 2.6	6300	1.1	1.2	0.17/1.4 ( $H\beta$ )
J1232+0912	2020 Jun 5	OSIRIS	Hn4/(16520–17370)	2.8 $\times$ 2.8	5400	1.2	1.0	0.22/1.8 (tip/tilt star)
J1550+0806	2021 May 3	OSIRIS	Hn5/(17210–18080)	1.7 $\times$ 2.4	8100	1.2	0.4	0.23/1.9 (tip/tilt star)
J1604+5633	2021 May 4	OSIRIS	Hn5/(17210–18080)	1.7 $\times$ 2.4	3600	1.3	1.2	0.22/1.8 (tip/tilt star)
J1652+1728	2019 May 7; 2019 May 8	NIFS	K/(19900–24000)	2.6 $\times$ 2.8	6000	1.1; 1.1	0.4	0.20/1.6 (continuum)
J2223+0857	2018 Sep 1	OSIRIS	Hn3/(15940–16760)	2.5 $\times$ 2.8	7200	1.2	0.6	0.19/1.6 (tip/tilt star)
J2323-0100	2017 Aug 13; 2018 Aug 11	OSIRIS	Hn4(16520–17370)	2.6 $\times$ 2.8	18000	1.1; 1.1	0.5; 0.6	0.15/1.3 (tip/tilt star)

<sup>a</sup>The effective useful co-added field of view.

<sup>b</sup>FWHM obtained from fitting the Gaussian core of the PSF. The corresponding physical scale at the redshift of the target is also reported.

physical interpretation of all the [O III] kinematic components as a sample.

### 3.1 Narrowband Images and Integrated Spectra

While the NIFS data are broadband, the OSIRIS targets were observed through narrowband filters of widths (83–88)  $\text{\AA}$ , which do not cover the entire  $H\beta$ -[O III] region. We therefore utilize the broadband longslit data and the best fits from Perrotta et al. (2019) to inform de-blending of the data into different emission components and therefore generation of narrowband continuum and [O III] images from the OSIRIS data cubes. For J2223+0857 which is not part of the longslit sample, the bulk of  $H\beta$  emission is fortunately cleanly separated from [O III] and we can therefore perform a fit to the OSIRIS spatially-integrated spectrum. We fit a constant to the continuum, a single Gaussian to  $H\beta$ , and two double Gaussians that are tied in kinematics and 1:3 amplitude ratios to [O III]  $\lambda\lambda 4959, 5007$ . These are the least number of components that best fits the spatially-integrated spectrum of J2223+0857.

From the fits to the longslit spectra or the spatially-integrated OSIRIS spectrum we can then identify wavelength channels that are blend of ( $H\beta$ +continuum), blend of ( $H\beta$ +[O III]+continuum), blend of ([O III]+continuum), and pure continuum. From each data cube,

we create a continuum flux map by summing wavelength channels that are identified to contain purely continuum and channels that contain  $H\beta$  plus continuum emissions, as shown in the first column of Fig. 2. This is done to increase the S/N of this narrowband image by relying on the assumption that  $H\beta$  is spatially unresolved, justified on the measured sub-parsec sizes of quasar broad-line regions (see Williams et al. 2017) while neglecting the narrow-line region component by necessity. The maps are spatially smoothed with a Gaussian kernel of FWHM 0.1 arcsec and we mark contours of S/N of two to aid visualization of the ERQ emission. We determine S/N from the data and variance channels containing purely continuum/ $H\beta$  as delineated in the integrated spectra shown in the third column of Fig. 2, ignoring strong sky emissions and filter edges. From each data cube, we create an [O III] map from summing wavelength channels that contain [O III]  $\lambda\lambda 4959, 5007$  emission and subtract the continuum and any blending  $H\beta$  emission, as shown in the second column of Fig. 2. The continuum level of each spaxel is approximately constant across the narrowband and is determined by the two-sigma-clipped mean of the channels used to generate the continuum map. The blending  $H\beta$  emission flux relative to continuum level is determined from the longslit best-fit, relying on the assumption that  $H\beta$  is spatially unresolved. The maps are spatially smoothed and we mark contours of S/N of two to aid visualization. We determine S/N from channels

containing [O III] as delineated in the integrated spectra, ignoring strong sky emissions and filter edges.

From each data cube, we create a spatially-integrated spectrum by summing all spaxels of S/N greater than two over the full wavelength range, as shown in the third column of Fig. 2. We mark wavelength boundaries between (H $\beta$ +continuum), (H $\beta$ +[O III]+continuum), ([O III]+continuum), and continuum-only emissions. With these clearly delineated wavelength regions, we ensure that no [O III]-containing channels contribute to the continuum flux maps in the first column of Fig. 2. Where a longslit spectrum exists, we overplot it to give context to the narrowband spectrum. The small discrepancy between the OSIRIS spatially-integrated spectra and the longslit spectra comes from the different physical regions extracted. The OSIRIS spatially-integrated spectra only include S/N > 2 spaxels while the longslit spectra are 0.7-arcsec extractions. For J2223+0857 which does not have a longslit spectrum we overplot our best fit and separately show the H $\beta$  and the two individual [O III] components.

Since a longslit spectrum of J2223+0857 has not been previously obtained, we measure its [O III]  $\lambda$ 5007 emission-line properties from the OSIRIS spatially-integrated spectrum to put it in context with the other ERQs. We calculate the  $v_{98}$  and the  $w_{80}$  values to quantify the kinematics as in Perrotta et al. (2019). We define  $v_{98}$  as the velocity that encompasses 98% of the line flux integrating from the red end, which is a measure of the maximum outflow velocity traced by an emission line. We define  $v_{50}$  as the line centroid, and is a measure of the bulk velocity of the line-emitting gas. We define  $w_{80}$  as the velocity width that encompasses 80% of the line flux around the centroid and excludes 10% of the red and blue wings, which is often used to find signature of AGN-driven outflows, and similarly we define  $w_{90}$ . The non-parametric  $v_{98}$ ,  $v_{50}$ ,  $w_{80}$ , and  $w_{90}$  values of the total [O III]  $\lambda$ 5007 emission derived from our best-fit are respectively  $(-7690 \pm 300) \text{ km s}^{-1}$ ,  $(-5510 \pm 200) \text{ km s}^{-1}$ ,  $(6030 \pm 170) \text{ km s}^{-1}$  and  $(7760 \pm 320) \text{ km s}^{-1}$ . These values make the [O III] kinematics of J2223+0857 typical of the ERQs measured in the longslit sample. The rest equivalent width and the line luminosity of the total [O III]  $\lambda$ 5007 emission derived from our best-fit are respectively  $(139 \pm 5) \text{ \AA}$  and  $(4.2 \pm 0.1) \times 10^{43} \text{ erg s}^{-1}$ , again typical of other measured ERQs.

Fig. 2 reveals that in J0006+1215, J1217+0234, J1232+0912, and J2323–0100 there exists continuum emission not consistent with a point-spread function. Four sources of this sample, namely J1217+0234, J1232+0912, J1652+1728, and J2323–0100, overlap with the Zakamska et al. (2019) sample of Hubble Space Telescope (HST) near-IR images that correspond to the rest-frame  $B$ -band and do not cover [O III]  $\lambda$ 4959,5007. For J0006+1215, the OSIRIS narrowband images reveal very extended continuum and [O III] emissions. The analysis of Section 3.2 will show that the extended [O III] likely traces dynamically quiescent interstellar media, supporting the extended continuum being diffuse starlight. For J1217+0234, in the OSIRIS images we find spatially-resolved, clumpy, disturbed continuum and [O III] emissions. The HST image reveals extended continuum emission around this source out to 3 arcsec, with the larger detectable extent due to higher surface brightness sensitivity. Section 3.2 will show that the extended [O III] is likely interstellar media. The HST image and the extended quiescent [O III] both support the extended continuum detected in OSIRIS data being diffuse starlight. For J1232+0912, in the OSIRIS image we find a hint of extended continuum. The HST image reveals extended continuum emission around this source out to 3 arcsec at higher sensitivity. The HST image independently confirms the extended continuum detected in OSIRIS data being diffuse starlight. For J2323–0100, a second nucleus is marginally discernible 1.3 arcsec away in the north-northeast

direction. The HST image reveals the ERQ is in an ongoing major merger with a second nucleus at that position. We note that for J1652+1728, although extended continuum is not detected in the NIFS data, the HST image finds extended continuum around the source out to 6 arcsec. Overall we identify signs of merger activities in ERQs corroborated by findings from HST images, although we do not attempt to explore systematic uncertainties and observational biases to quantify a merger fraction (see Villforth 2023).

### 3.2 Surface brightness radial profiles

The first technique of assessing extended emissions consists of comparing the surface brightness radial profiles of the continuum and [O III] emissions of the ERQ with a reference PSF. For each ERQ, we extract a nuclear spectrum from an aperture of radius 0.1 arcsec centred at the centroid of the ERQ emission, and extract from annular apertures of progressively larger radii till reaching the edges of the field of view. The annular apertures have variable widths of 0.1 arcsec to 0.4 arcsec, allowing finer spatial sampling in the inner regions and increasing S/N of low surface brightness emissions in the outer regions.

We first perform continuum and line fitting to the nuclear spectrum. Due to the limited wavelength range of the OSIRIS data, in most ERQs either the continuum redward of [O III] or the H $\beta$  emission is well covered, but not both. We therefore employ the best-fit parameters to the broadband longslit data of Perrotta et al. (2019) to inform our line fitting. We do not force our line decomposition to precisely follow the longslit results, as the precise spectral profile depends on the regions included in the extraction aperture (Law et al. 2018). We use a constant to fit the continuum, as the continuum is approximately flat within a limited wavelength range and linear function would introduce too many degrees of freedom for a fit to be successful. Where the H $\beta$  peak is not covered we fix the H $\beta$ -to-continuum amplitude ratio to the longslit value and allow the flat continuum level to vary in the fitting process, relying on the assumption that H $\beta$  is spatially unresolved. Where the H $\beta$  peak is covered we allow both the flat continuum level and the H $\beta$  amplitude to vary. We use one to two Gaussians to fit H $\beta$ , and two to three double Gaussians tied in kinematics and amplitude ratios of 1:3 to fit [O III]  $\lambda$ 4959,5007. The number of components follows the longslit results and is also motivated by their distinct spatial distributions which give rise to physical meaning, which is further described in Section 3.4. The change in  $\chi^2$  is minimal if we increase the number of fitted components and we prefer the least number of [O III] components per ERQ system that best fits the data. We initialize the free [O III] kinematic parameters to the longslit values, and fix the H $\beta$  kinematic parameters to the longslit values. It has been found from the longslit sample that Fe II contribution does not significantly change the [O III] measurements (Perrotta et al. 2019). We then fit other annular aperture spectra. We determine the H $\beta$ -to-continuum amplitude and fix the H $\beta$  kinematic parameters in the same way as in the nuclear spectrum. With the exception of J1031+2903, we fix the [O III] components' kinematics to the nuclear spectrum's results freeing only their tied amplitudes. For J1031+2903 whose second [O III] component is most apparent in the (0.2–0.4) arcsec annulus, we fix the second [O III] component's kinematic parameters in all apertures to this annulus's results (we note that the reduced  $\chi^2$  values of including or excluding the second [O III] component in the nuclear spectrum are nearly equivalent). This is done to reduce the degrees of freedom in fitting low S/N data. For each extracted aperture spectrum we keep a component as a detection if its fitted flux is above  $2\sigma$ . We find that the same two to three [O III] kinematic

components can be employed to produce reasonable fits across all apertures. We order the components by their velocity dispersion values from high to low and name them “component 1”, “component 2”, and “component 3” accordingly. Table 3 presents the velocity centroids and dispersions of these fitted [O III] components, and their formal  $\chi^2$  minimization errors. All ERQs but J1652+1728 are fitted with two [O III] components while J1652+1728 is fitted with three. A commonly adopted threshold for ionized outflows that require active galactic nucleus (AGN) driving is velocity dispersion  $\geq 250 \text{ km s}^{-1}$ , as these velocities are ten times more prevalent in AGN-host galaxies than star-forming galaxies (Harrison et al. 2016; Kakkad et al. 2020). With respect to this reference value, components 1 of all 10 ERQs are broad, tracing AGN-driven outflows, while components 2 and 3 are a mix of six broad and five narrow widths, with narrow widths tracing the more quiescent interstellar media. The five fitted components that are below the AGN-driven outflow cut are the component 2 of J0006+1215, J0209+3122, J1031+2903, J1217+0234 and the component 3 of J1652+1728. Among them, J0006+1215 and J1217+0234 have independent accurate systemic redshift measurements from CO host emission (Gillette et al. 2024). The narrow component 2 of both of them are fitted with zero velocity shift from the systemic, indicating that they trace quiescent interstellar media likely in dynamical equilibrium with their host galaxies. For a non-parametric reference, Table 4 presents the  $w_{80}$  value of the total [O III]  $\lambda 5007$  line profile in all extracted aperture spectra.

With the continuum and [O III] line fluxes derived from these spectral fits, we construct their surface brightness radial profiles as functions of the annular aperture radii. We determine errors on the radial profiles as propagated from the formal  $\chi^2$  minimization errors of the fitting the components. We also construct surface brightness radial profiles of the tip/tilt stars. We generally use tip/tilt stars rather than the extracted ERQ  $H\beta$  emission as the PSF model even though the broad-line region is spatially unresolved because tip/tilt stars have higher S/N. Exceptions are J1217+0234 where the tip/tilt star observations are noisy and we instead use the ERQ  $H\beta$  for describing the PSF, and J1652+1728 where we use the ERQ’s spatially-unresolved continuum in the NIFS data for consistency with Vayner et al. (2021a). Fig. 3 presents these nuclear and annular aperture spectra, their best fits, and the surface brightness radial profiles. We qualitatively assess whether the continuum and the [O III] components are spatially resolved by comparing with their reference PSF profiles. We also quantitatively assess spatial extents by calculating the half-light radii and our defined maximum radii that respectively encompass 50% and 90% of the fluxes of the different emission components. We determine their errors as propagated from the formal errors of the fitted components. Table 5 presents these characteristic  $R_{\text{half}}$  and  $R_{\text{max}}$  sizes of the continuum, total [O III], and the individual [O III] components. We report radii that are deconvolved with their reference PSFs, and for unresolved emission components we report their upper limit at the PSF sizes. As the adaptive-optics-corrected PSF involves a Gaussian-like core and a weak halo comparable to the natural seeing (Law et al. 2018), the half-light radii better characterize the emission component sizes. The maximum radii, on the other hand, are more commonly reported in the literature, hence calculating them enables comparison with measurements on other luminous quasars.

The continuum emissions of J0006+1215, J1232+0912, J1217+0234, and J1604+5633 are spatially resolved, although we caution the suboptimal weather of the J1604+5633 observations. In particular the continuum emission of J0006+1215 remains detectable out to edge of the field at 1.4 arcsec.

Majority of the [O III] components that exceed the AGN-outflow

threshold are spatially unresolved. Specifically, among all [O III] components of the sample that meet the AGN-outflow cut, only five out of 16 of them are spatially resolved, namely the J1550+0806 component 2, the J1652+1728 components 1 and 2, and the J2323–0100 components 1 and 2. These five components are spatially compact with maximum radii  $\leq 4 \text{ kpc}$ . On the contrary, all five components of the sample that are below the AGN-outflow cut are spatially resolved, namely the component 2 of J0006+1215, J0209+3122, J1031+2903, J1217+0234 and the component 3 of J1652+1728. The narrow component 2 of J1031+2903 is not centrally concentrated but displays a local dip in its surface brightness radial profile at (0.2–0.4) arcsec, implying clumpiness in the interstellar media. While the detected extent of an individual emission component can be moderated by dust extinction, we observe a general trend for the sample that narrower, more extended components become more prominent in outer annuli relative to broader, more compact components.

### 3.3 Residuals of PSF subtraction

The second technique of assessing extended emissions consists of generating the residual data after subtracting the nuclear spectrum spaxel by spaxel following a two-dimensional empirical PSF profile. The PSF on the OSIRIS detector varies by only a few tenths of a pixel as a function of lenslet or wavelength (Lockhart et al. 2019). For a spatially unresolved emission component, e.g. the quasar broad line region or continuum, the spectral shape anywhere in the data cube would be about the same as that at the quasar centroid modulo a flux scaling factor. With this, an emission component that does not follow the nuclear spectral shape is revealed to be spatially resolved. We use the nuclear spectrum of radius 0.1 arcsec to be the spatially-unresolved quasar spectral template, and determine the continuum or fitted  $H\beta$  flux level where it is well covered. For every spaxel in the data cube, we re-scale the normalization of this unresolved template to match the continuum or  $H\beta$  flux and subtract it. We conservatively err on the side of over-subtraction to ensure that residual emission is not the PSF wings. This method is not sensitive to revealing extended continuum emissions and we only assess extended line emissions. Due to the limited wavelength coverage and data sensitivity, we do not attempt a more complex PSF decomposition treatment.

To generate the residual surface brightness map of each ERQ, we collapse the PSF-subtracted data cube along the wavelength dimension and spatially smooth with a Gaussian kernel of FWHM 0.1 arcsec and mark contours of S/N of two. We determine S/N from the PSF-subtracted data channels and their corresponding variance channels and the variance channels of the nuclear spectra that form the PSF templates. From the PSF-subtracted data cube we extract from annular apertures of progressively larger radii till the edges of the field. We fit two to three [O III] components to the residual annular spectra with the same kinematic parameters as before PSF subtraction and allowing the amplitudes to vary. We then calculate the half-light and maximum radii from the fitted [O III] fluxes in the annular bins. Because the residual emission tends to be either dominated by one component where the individual components are physically distinct, or have very similar contribution from two components where they are broad and blended, we only report the total [O III] profile’s characteristic sizes. We determine their errors as propagated from the formal  $\chi^2$  minimization errors of the components fitted to the PSF-subtracted residual data. Fig. 4 presents these residual surface brightness maps, residual annular aperture spectra, and their best fits. Brightness flares near the edges of the field of view should be considered together with the presence of emission-line shapes in the outer annular spectra to assess detection. Table 6 presents the half-

light and maximum residual [O III] radii. With the PSF subtraction method we reveal spatially resolved [O III] emission in J0006+1215, J0209+3122, J1031+2903, J1217+0234, J1550+0806, J1652+1728, and J2323–0100, totalling seven out of 10 ERQs. In J0006+1215, J0209+3122, J1031+2903, and J1217+0234, the residual emission is dominated by a narrow component. In J1550+0806, the residual emission is dominated by a component that has the lowest velocity dispersion of all ERQ fitted components that meet the AGN-outflow cut. In J1652+1728, the residual emission is dominated by a narrow component and a component that has the second lowest velocity dispersion of all components that meet the AGN-outflow cut. In J2323–0100, where we detect residual emission contributed by both components 1 and 2 which both meet the AGN-outflow cut, we have the best corrected angular resolution and the deepest observations. We note the hints of one or two ionization cones in J0006+1215, J1217+0234, J1550+0806, and J1652+1728.

### 3.4 Physical Motivation of the [O III] Components

For a spatially-integrated spectrum, fitting Gaussians provides a noiseless approximation to the line profile and the individual components are not physically motivated models. The situation is however different for integral-field spectroscopy at high spatial resolution. Despite the arbitrary nature of Gaussian line profiles, when the individual kinematic components of a source can be coherently fitted across many spatial resolutions and have different spatial distributions, the individual components can be ascribed to distinct dynamical mechanisms. Nonetheless, considering the results from sensitive JWST NIRSpec integral-field spectra of J1652+1728, interpreting individual kinematic components averaged over large apertures especially when galaxies are in mergers and have various clumps is non-trivial (Wylezalek et al. 2022). We therefore also examine the velocity centroid distribution, velocity dispersion distribution, and spatial extent distribution of all components. We then consider components 1 and 2 physically distinct in J0006+1215, J0209+3122, J1031+2903, J1217+0234, and J1550+0806, and components 1, 2, and 3 distinct in J1652+1728. On the other hand, when two components of a source are both broad, blended, and have very similar spatial distributions, often times both spatially unresolved, only the sum of the Gaussians is meaningful as a quantification of the total outflow line profile (Zakamska & Greene 2014). We therefore do not consider components 1 and 2 physically distinct in J1232+0912, J1604+5633, J2223+0857, and J2323–0100.

From our radial profile analysis and PSF subtraction analysis, we find that all narrow [O III] components of velocity dispersions below  $250 \text{ km s}^{-1}$  are spatially resolved, while broad [O III] components are a mix of spatially resolved and unresolved. We can demonstrate this finding is not sensitive to the defined AGN-driven outflow threshold. Fig. 5 presents the histogram of velocity dispersions of all fitted [O III] components. A trough in the distribution of velocity dispersions is present at  $\sim(250\text{--}400) \text{ km s}^{-1}$ . Thanks to the adaptive optics observations we are able to ascribe physical meaning to the narrow versus broad components, which was previously not possible with longslit data whose line profile decomposition may be arbitrary. The bimodal distribution justifies the adopted AGN-outflow threshold, and the precise velocity cutoff on AGN-driving does not affect the discussion in Section 4 comparing the [O III] spatial extents with other AGN-driven outflows in the literature. Further, the bimodal distribution implies that the narrow and broad components likely have distinct dynamical mechanisms, with narrow components possibly tracing the more quiescent interstellar media. We note that in ERQs where both fitted components are broad and blended, the individual

components are not physically distinct but represent lower limits to the velocity widths of the fast outflowing features. The histogram of kinematic components thus underestimates the true velocity distribution of fast outflowing materials, and the actual distinction between narrow versus broad [O III]-emitting gas should be even more prominent.

In the analysis of JWST NIRSpec integral-field spectra of J1652+1728 in Vayner et al. (2023) that measure diffuse [O III] out to 2 arcsec from the central quasar, they find a similar bimodal distribution in the velocity dispersions of components fitted to this single system. This further attests to the physical motivation of the [O III] components when the data has sufficient angular resolution.

## 4 DISCUSSION

We assess the implications of our measured [O III] emitting region sizes and spatially-resolved kinematics of ERQs by comparing them with other non-jetted/radio-quiet and intrinsically luminous quasars at similar redshifts. The radio requirement on the control samples is to ensure comparing radiation-driven rather than jet-driven outflows. The luminosity requirement is to control for the quasar narrow-line region’s size-luminosity relation (e.g. Liu et al. 2013; Sun et al. 2017). Although the bolometric luminosities of ERQs are only estimates and uncertain by at least a factor of 2 (Hamann et al. 2017), our goal is not to look for luminosity trends but merely select comparably luminous quasars. The redshift requirement is to control for cosmic evolution. To minimize biases in comparing low surface brightness emissions, we only select control samples from (8–10) m class adaptive-optics or JWST NIRSpec integral-field observations. Given that the outflow extent in J1652+1728 measured in NIFS data is much smaller than that measured with JWST, we measure sizes in JWST observations of the comparison sources only down to the typical surface brightness sensitivity of adaptive-optics observations which is about two orders of magnitude lower. From the Kakkad et al. (2020) adaptive-optics sample we select 11 well-measured normal blue quasars, and we select the Williams et al. (2017) adaptive-optics observations of a blue quasar, the Perna et al. (2023) JWST NIRSpec observations of a blue quasar, and the Brusa et al. (2016) adaptive-optics observations of a Type II narrow-line quasar.

### 4.1 Compact ERQ-driven [O III] Outflows

We compare the maximum radii of AGN-driven outflows in ERQs and other luminous quasars. For each ERQ, we calculate the maximum radius of AGN-driven outflows as the maximum radius of component 1 or the maximum radius of the total of components 1 and 2 depending on whether one or both components meet the velocity dispersion  $\geq 250 \text{ km s}^{-1}$  cut. The maximum radii of AGN outflows remain unchanged if we instead apply a corresponding  $w_{80} \geq 600 \text{ km s}^{-1}$  cut on the total [O III]  $\lambda 5007$  line profile. For the comparison sources, the maximum radii are not always explicitly reported in the literature, we therefore measure the maximum radii from the published emission-line maps. Where the [O III] emission is spatially resolved we measure the maximum radius of a S/N > 2 spaxel that meets the same AGN-outflow cut, and where the emission is unresolved we adopt a 0.5 arcsec upper limit informed by the typical adaptive optics correction performance. Fig. 6 presents the maximum radii of AGN-driven [O III] outflows versus bolometric luminosities of ERQs and other radio-quiet, luminous, cosmic noon quasars in the literature. There is a hint that ERQ-driven outflows are more spatially compact than other luminous quasars. Using the

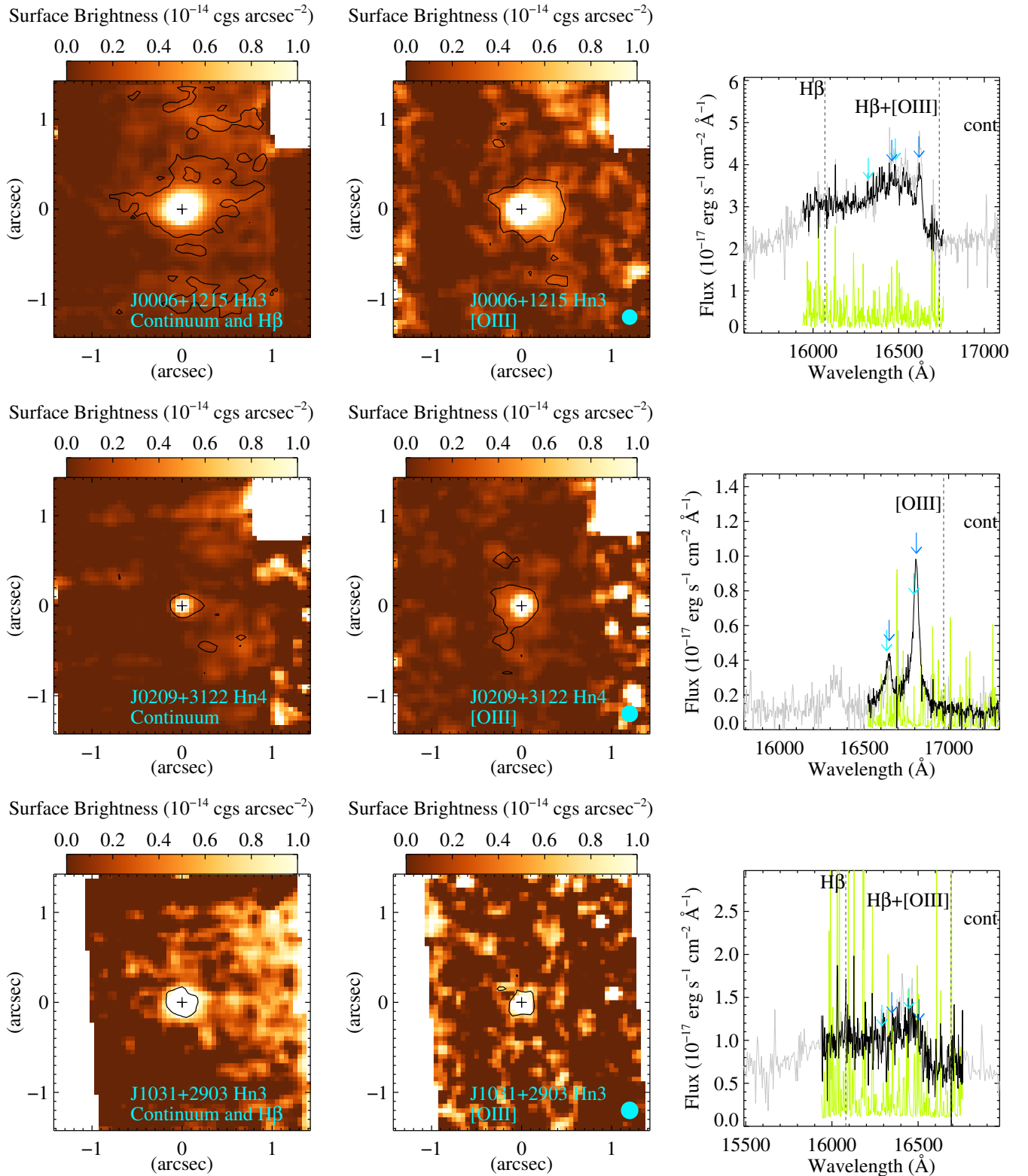


**Figure 2.** Narrowband images and integrated spectra for visualizing adaptive optics observations of the ERQ sample. The first column is surface brightness maps summing channels of continuum and H $\beta$  emissions. The second column is surface brightness maps summing channels of [O III] emission and subtracting continuum and any blending H $\beta$  emissions. Contours of S/N of two are marked on the maps. The Gaussian FWHM size of the PSF is shown as a circle on the [O III] map. The third column is spatially-integrated spectra summing spaxels of S/N greater than two shown in observed wavelengths. The flux is in black and the 1- $\sigma$  error is in lime. Boundaries of H $\beta$ , [O III], continuum emissions and their blends are marked on the spectra. We overplot a previously published longslit spectrum in grey where it exists. For J2223+0857 which does not have a longslit spectrum, we overplot our best fit and the H $\beta$  and the two [O III] components in orange, lime, cyan, and blue, and show the residual spectrum.



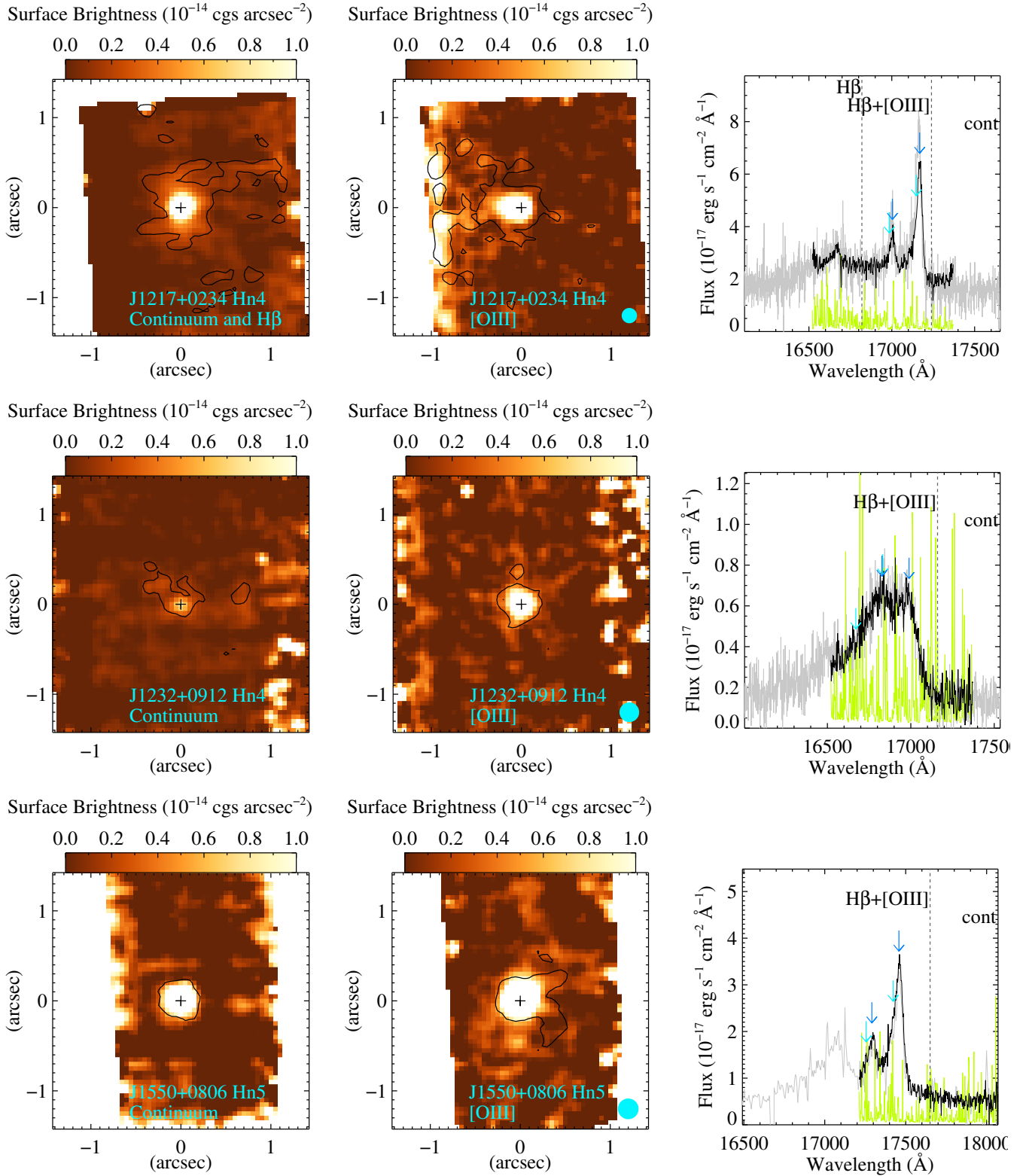


Figure 2 – continued

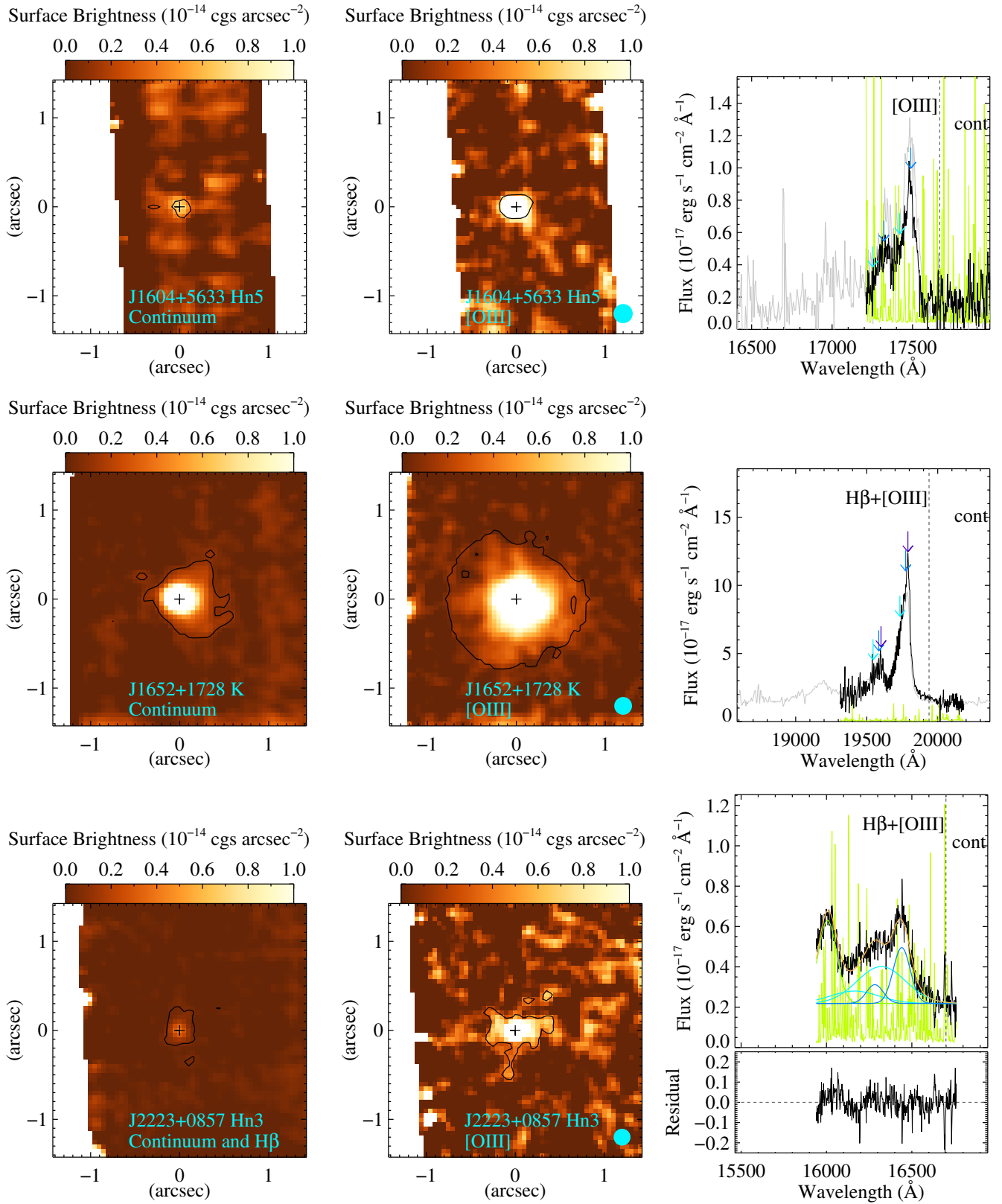


Figure 2 – continued

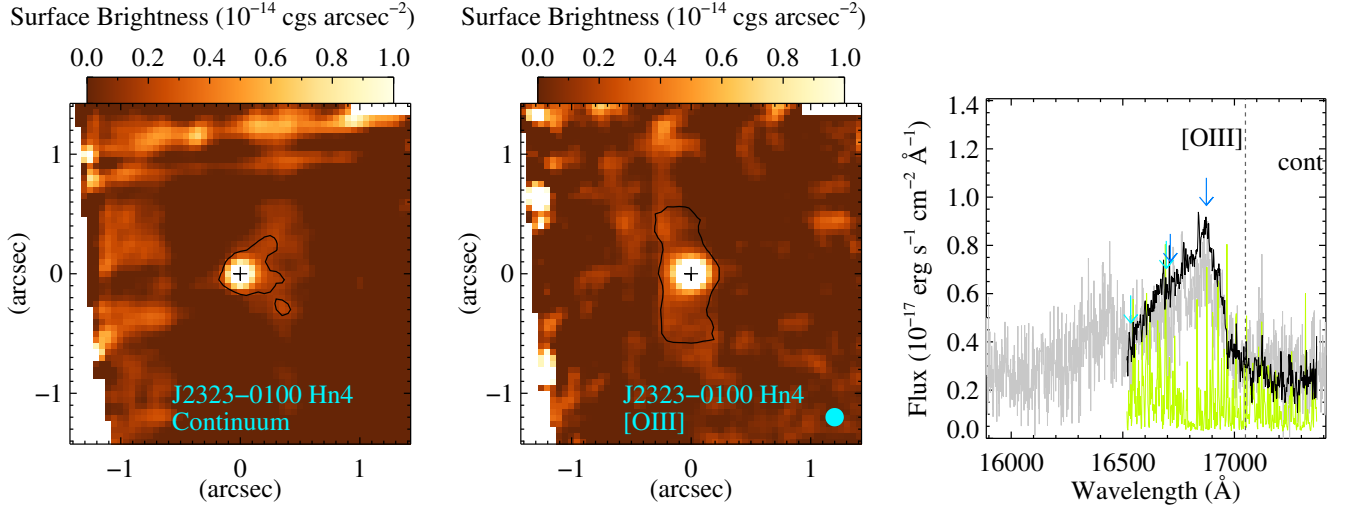


Figure 2 – continued

**Table 3.** Kinematic Parameters of Fitted [O III] Components (fixed across all extracted apertures)

Name	[O III] Comp1 Velocity Centroid (km s <sup>-1</sup> )	[O III] Comp1 <sup>a</sup> Velocity Dispersion <sup>b</sup> (km s <sup>-1</sup> )	[O III] Comp2 Velocity Centroid (km s <sup>-1</sup> )	[O III] Comp2 <sup>a</sup> Velocity Dispersion <sup>b</sup> (km s <sup>-1</sup> )	[O III] Comp3 Velocity centroid (km s <sup>-1</sup> )	[O III] Comp3 <sup>a</sup> Velocity Dispersion <sup>b</sup> (km s <sup>-1</sup> )
J0006+1215	-2485±51	1997±103	0±30	221±41	/	/
J0209+3122	-554±19	998±103	-286±18	237±18	/	/
J1031+2903	-1050±51	1100±57	0±21	201±29	/	/
J1217+0234	-340±33	530±18	0±17	142±29	/	/
J1232+0912	-3870±32	1872±18	-1117±18	979±18	/	/
J1550+0806	-2565±47	1200±18	-1952±17	443±17	/	/
J1604+5633	-1126±41	1174±18	+55±17	525±17	/	/
J1652+1728	-1101±34	919±23	-492±17	500±18	-250±33	100±31
J2223+0857	-2876±58	2612±72	-682±18	907±25	/	/
J2323-0100	-4142±105	1782±72	-990±30	1253±29	/	/

<sup>a</sup>We order the components by their velocity dispersion values from high to low.

<sup>b</sup>We define the threshold for outflows that require AGN driving at velocity dispersion  $\geq 250$  km s<sup>-1</sup>.

**Table 4.**  $w_{80}$  Velocity Widths of Total [O III]  $\lambda 5007$  Line Profiles in Extracted Apertures

Name	(0.0–0.1) arcsec (km s <sup>-1</sup> )	(0.1–0.2) arcsec (km s <sup>-1</sup> )	(0.2–0.4) arcsec (km s <sup>-1</sup> )	(0.4–0.6) arcsec (km s <sup>-1</sup> )	Annulus 5 <sup>a</sup> (km s <sup>-1</sup> )	Annulus 6 <sup>b</sup> (km s <sup>-1</sup> )
J0006+1215	5170±130	5110±130	5060±180	4890±1070	570±110	/
J0209+3122	2060±20	2110±70	2150±350	610±10	610±10	610±10
J1031+2903	2790±90	2830±180	2550±280	/	/	/
J1217+0234	1290±40	1170±50	980±170	1020±130	1080±260	360±70
J1232+0912	5420±50	5330±130	5360±310	5230±3000	/	/
J1550+0806	2550±120	2480±120	2240±200	2730±1080	/	/
J1604+5633	2790±100	2640±290	1340±20	/	/	/
J1652+1728	2000±30	1940±40	1840±30	1800±50	1710±80	1180±520
J2223+0857	6090±200	6120±610	6180±1450	2330±60	/	/
J2323-0100	5570±80	5450±470	5620±810	5780±1360	/	/

<sup>a</sup>(0.6–1.0) arcsec for J0006+1215; (0.6–0.8) arcsec for the rest.

<sup>b</sup>(1.0–1.4) arcsec for J0006+1215; (0.8–1.2) arcsec for J1232+0912 and J1652+1728; (0.8–1.0) arcsec for the rest.

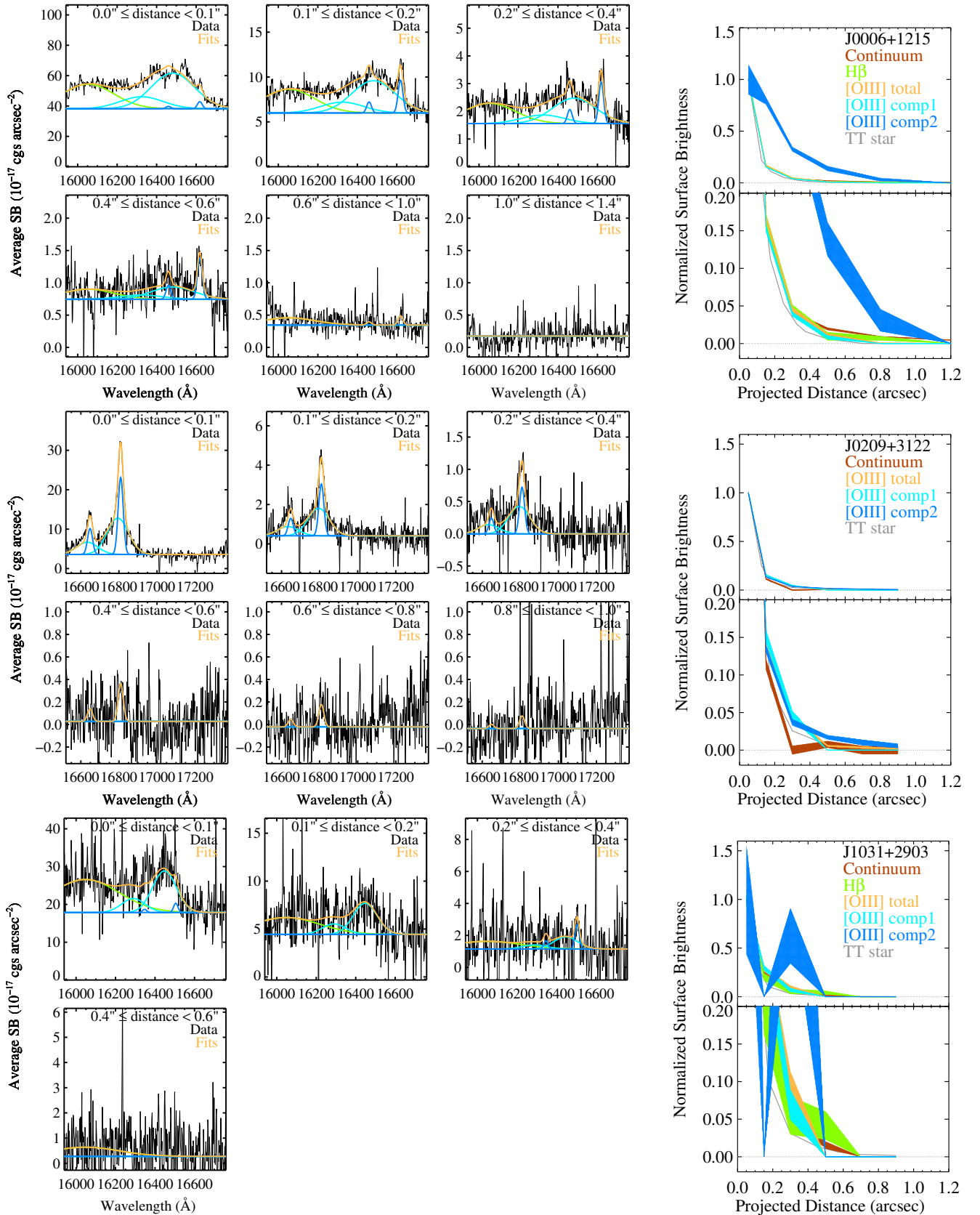


**Figure 3.** The left-hand panels show nuclear and annular spectra generated from OSIRIS and NIFS data of ERQs. We overplot the best-fits to the aperture spectra in orange. On each spectrum we overplot the H $\beta$  component in lime and the [O III]  $\lambda\lambda 4959, 5007$  components 1, 2, and 3 in cyan, blue, and indigo at the continuum level. The right-hand panels show the surface brightness radial profiles of the different emission components normalized to the brightest aperture, in two different zoom scales. Shown on the panels are the continuum emission in brown, H $\beta$  emission in lime, total [O III] emission in orange, [O III] components 1, 2, and 3 in cyan, blue, and indigo, and the tip/tilt star in grey. The shaded regions are the  $1-\sigma$  uncertainties in the surface brightnesses.

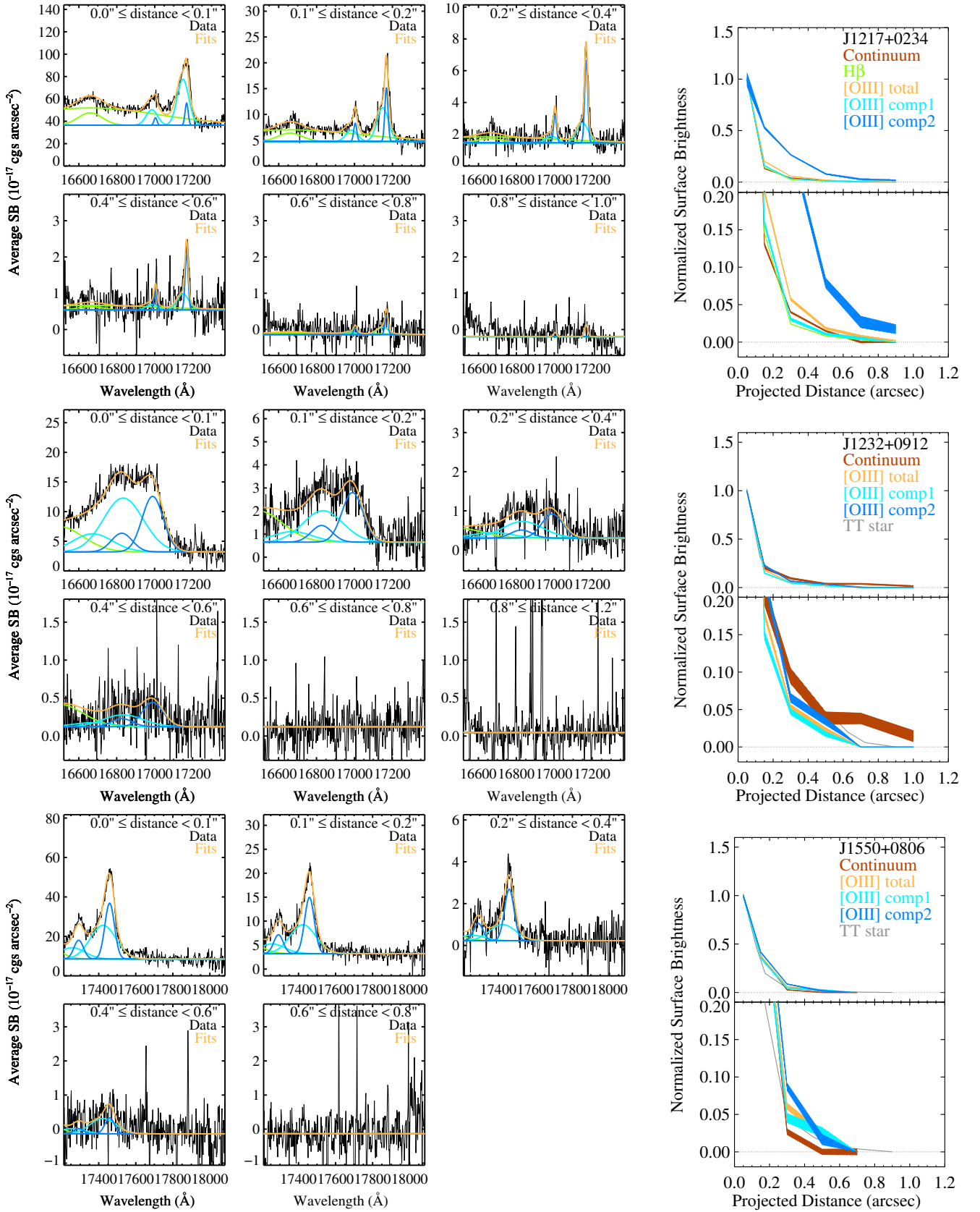


Figure 3 – continued

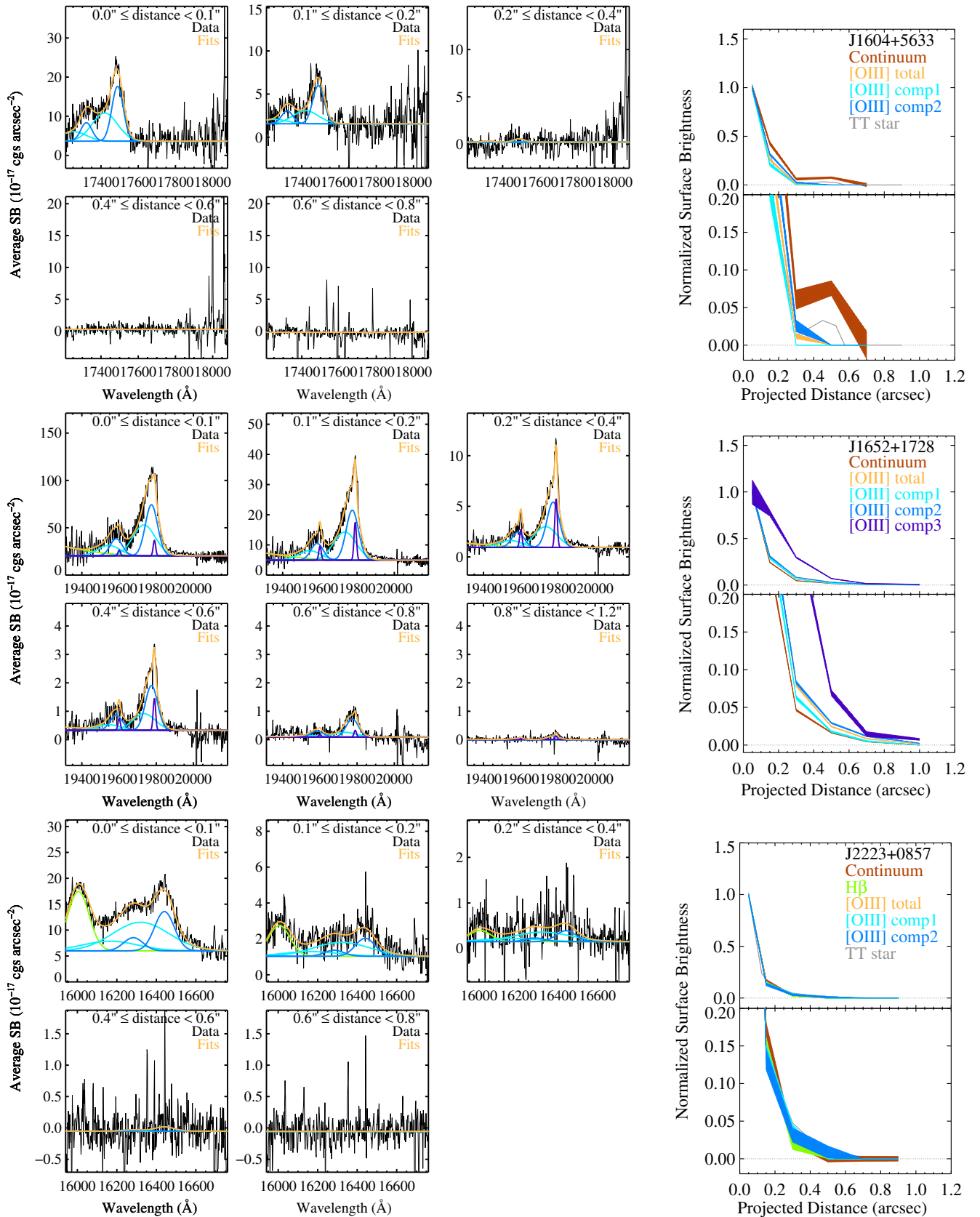


Figure 3 – continued

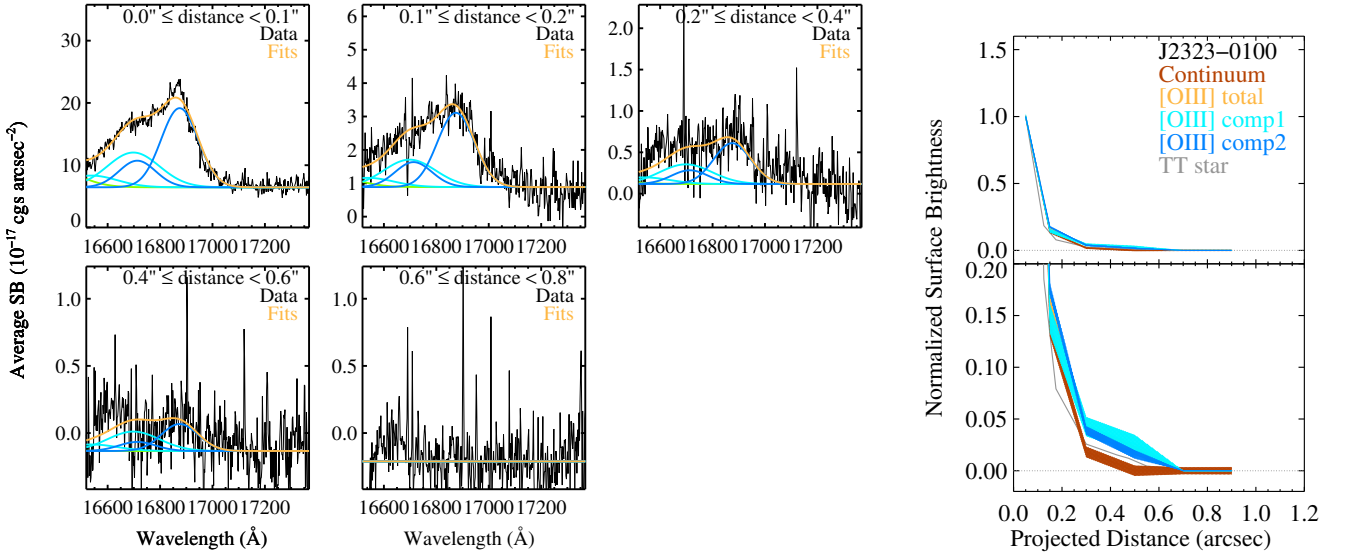


Figure 3 – continued

Table 5. Size Measurements from Surface Brightness Radial Profiles

Name	Cont. $R_{\text{half}}$ (kpc)	Cont. $R_{\text{max}}$ (kpc)	[O III] Comp1 $R_{\text{half}}$ (kpc)	[O III] Comp1 $R_{\text{max}}$ (kpc)	[O III] Comp2 $R_{\text{half}}$ (kpc)	[O III] Comp2 $R_{\text{max}}$ (kpc)	[O III] Comp3 $R_{\text{half}}$ (kpc)	[O III] Comp3 $R_{\text{max}}$ (kpc)	Total [O III] $R_{\text{half}}$ (kpc)	Total [O III] $R_{\text{max}}$ (kpc)
J0006+1215	>2.8	>8.9	<1.0	<3.0	$2.8 \pm 0.5$	$5.8 \pm 2.2$	/	/	<1.0	<3.0
J0209+3122	<1.1	<4.6	<1.1	<4.6	$1.7 \pm 0.5$	$4.6 \pm 2.3$	/	/	<1.1	<4.6
J1031+2903	<1.1	<4.5	<1.1	<4.5	$2.1 \pm 0.5^a$	<4.5	/	/	<1.1	<4.5
J1217+0234	$1.0 \pm 0.4$	<4.2	<1.0	<4.2	>2.5	>4.6	/	/	$1.4 \pm 0.4$	<4.2
J1232+0912	>3.4	>7.0	<2.2	<4.7	<2.2	<4.7	/	/	<2.2	<4.7
J1550+0806	<1.2	<3.9	<1.2	<3.9	$1.2 \pm 0.4$	<3.9	/	/	<1.2	<3.9
J1604+5633	$1.8 \pm 0.4$	<3.9	<1.1	<3.9	<1.1	<3.9	/	/	<1.1	<3.9
J1652+1728	<1.3	<4.2	<1.3	<4.2	$1.5 \pm 0.4$	$4.2 \pm 0.8$	>1.9	>4.2	<1.3	<4.2
J2223+0857	<1.3	<3.8	<1.3	<3.8	<1.3	<3.8	/	/	<1.3	<3.8
J2323-0100	<1.0	<3.6 <sup>b</sup>	$1.2 \pm 0.4$	<3.6	$1.0 \pm 0.4$	<3.6	/	/	$1.0 \pm 0.4$	<3.6

<sup>a</sup>If the marginally detected component 2 is treated as non-detection in the nuclear region, its  $R_{\text{half}}$  becomes 2.2 kpc with no change to other size measurements.

<sup>b</sup>A second nucleus is discernible at 1.3 arcsec away in the north-northeast direction despite the ERQ host continuum being spatially unresolved.

 Table 6. Size Measurements from PSF-subtracted Residuals<sup>a</sup>

Name	Total [O III] $R_{\text{half}}$ (kpc)	Total [O III] $R_{\text{max}}$ (kpc)
J0006+1215	$2.6 \pm 0.4$	$4.5 \pm 0.4$
J0209+3122	$1.5 \pm 0.5$	<4.6
J1031+2903	$1.9 \pm 0.4$	<4.5
J1217+0234	$2.6 \pm 0.4$	$6.5 \pm 0.8$
J1232+0912	<2.2	<4.7
J1550+0806	$2.5 \pm 0.4$	<3.9
J1604+5633	<1.1	<3.9
J1652+1728	$2.6 \pm 0.4$	$4.6 \pm 0.4$
J2223+0857	<1.3	<3.8
J2323-0100	$1.2 \pm 0.4$	<3.6

<sup>a</sup>Measured on the total [O III] profile after subtracting the PSF. Further information on the derivation of these quantities is available in Section 3.3.

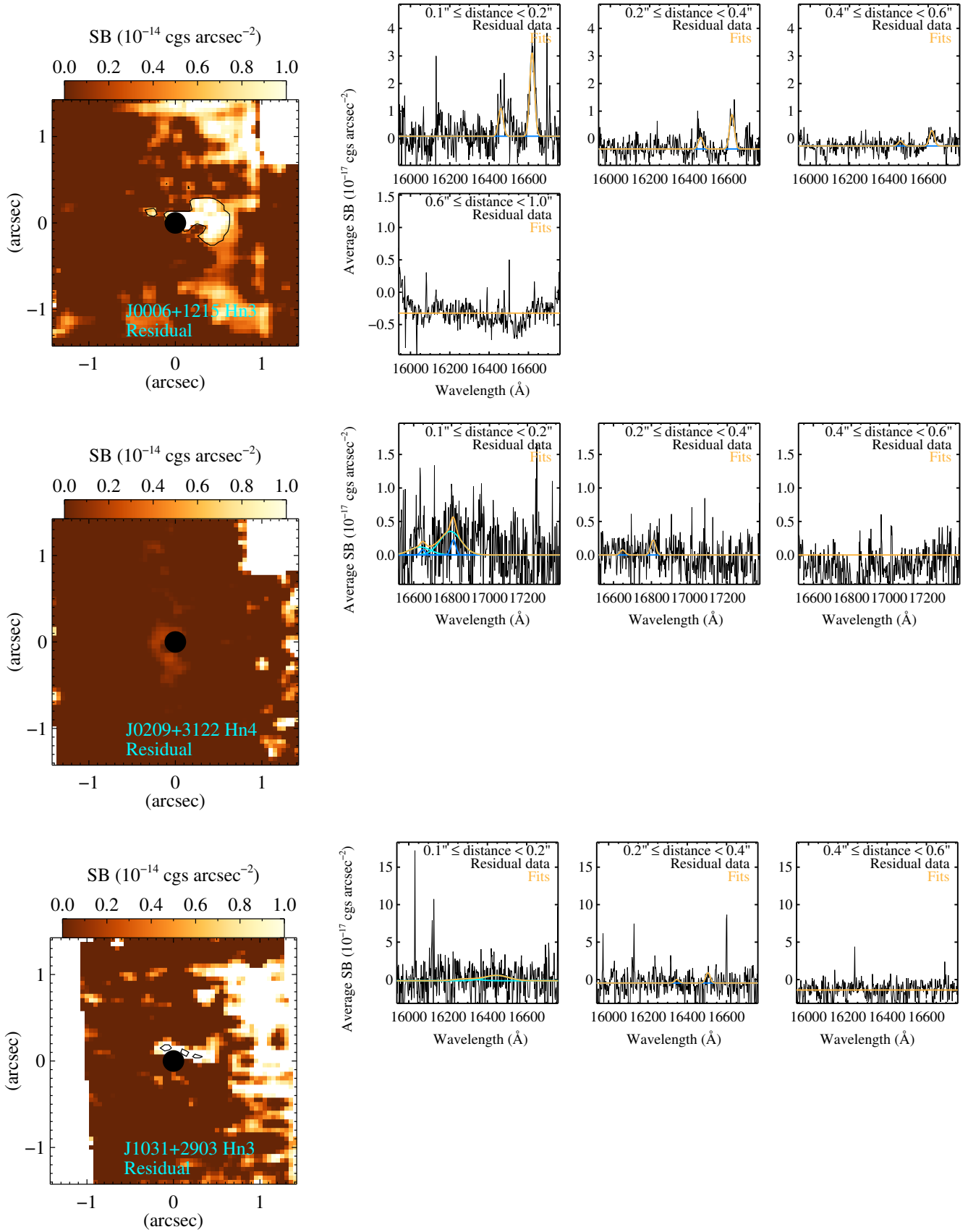


**Figure 4.** The left-hand panels show PSF-subtracted residual surface brightness maps summing all channels and the right-hand panels show the nuclear and annular aperture spectra generated from the PSF-subtracted residuals of the data cubes. We overplot the total best-fits to the aperture spectra in orange. On each spectrum we overplot the [O III] component 1 in cyan and the [O III] component 2 in blue at the continuum emission level.



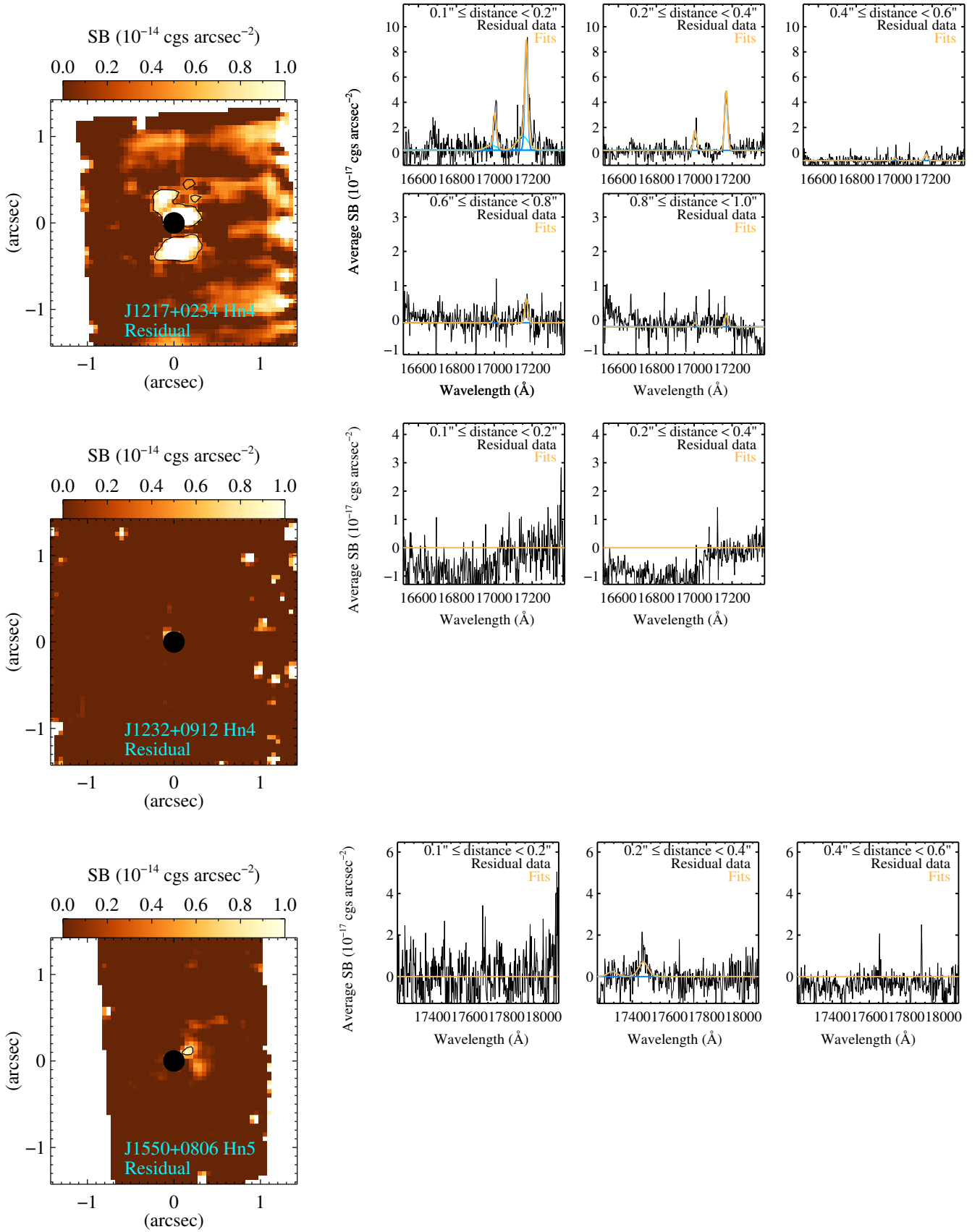


Figure 4 – continued

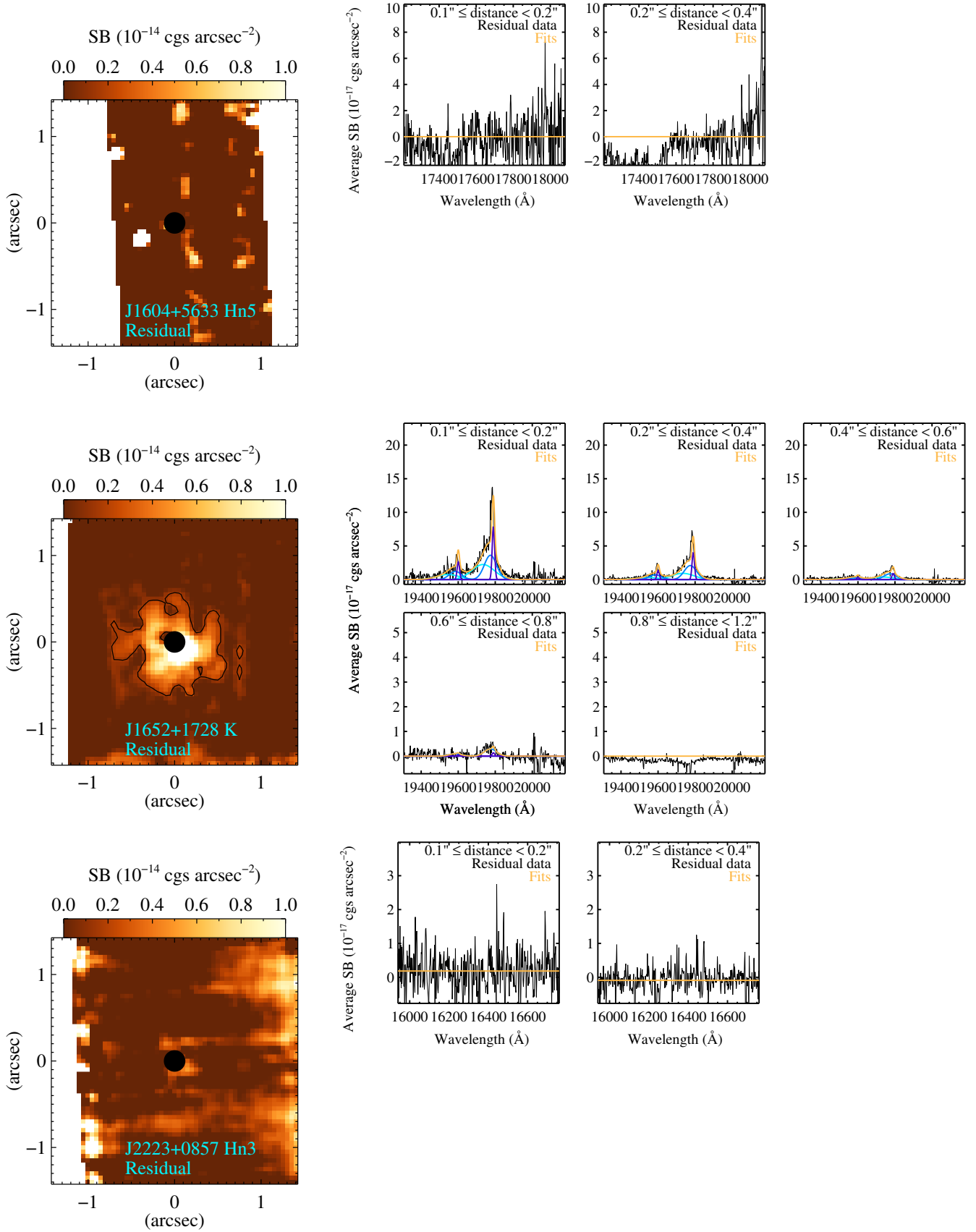


Figure 4 – continued

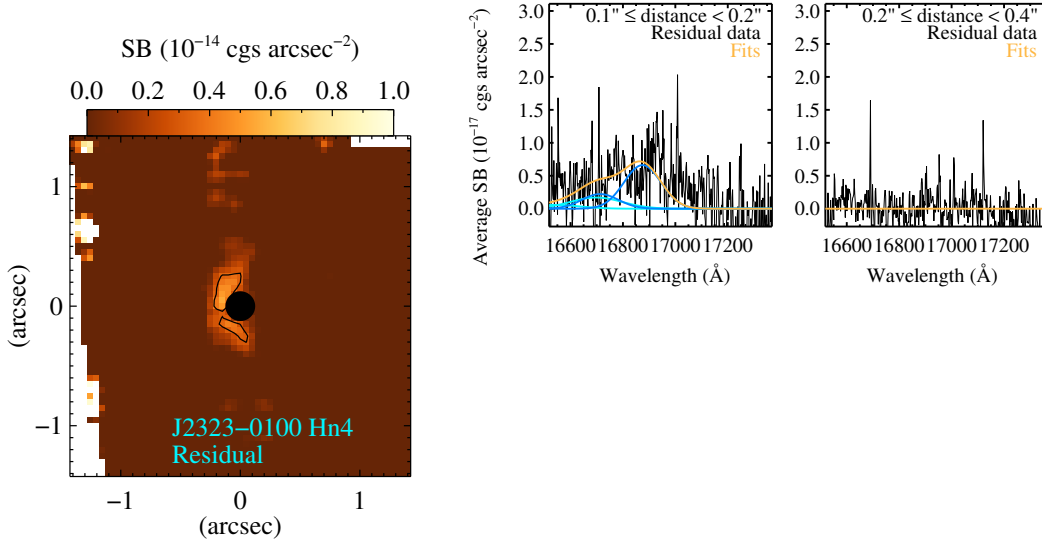
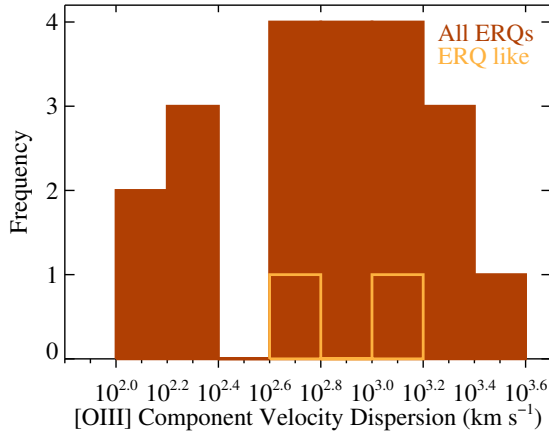


Figure 4 – continued



**Figure 5.** A histogram of the velocity dispersion of all [O III] components fitted to the ERQ sample. The full sample is shown in brown solid bars. Components of the one red ERQ-like quasar, J1550+0806, is separately shown in orange hollow bars.

ASURV software (Feigelson et al. 2014) we perform a two-sample Peto-Prentice test and find the probability that the ERQ distribution and the comparison quasar distribution are drawn from the same parent population is only 0.04. Since individually detected spaxels are less sensitive than annular averages, the maximum radius measurements of the comparison sources made on the maps should be considered conservative underestimates relative to the measurements on the ERQs encompassing 90% of the flux. While ERQs are on average extinct by three magnitudes in the rest-frame UV relative to a Type I spectral energy distribution (Hamann et al. 2017), ERQs are highly intrinsically luminous and their  $W3$ -band based bolometric luminosities are about an order of magnitude higher than the comparison samples. We therefore consider the size difference between ERQ-driven outflows and other AGN-driven outflows robust.

We also compare the half-light radii of the total [O III] emissions in ERQs versus the Kakkad et al. (2020) sample. The half-light radii of the total [O III] line profiles are less measurement-dependent than the maximum radii of AGN-driven [O III] outflows, and Kakkad et al. (2020) already have these measurements made and reported. Given the observed line profiles and the known relation between line velocity width and bolometric luminosity (e.g. Zakamska & Greene 2014; Sun et al. 2017), the AGN-driven outflows dominate the line fluxes and the extents of the total [O III] emissions largely trace extents of AGN-driven outflows. Fig. 7 presents the half-light radii of total [O III] emissions versus bolometric luminosities of ERQs and the luminous blue quasars from Kakkad et al. (2020). There is again a hint that the [O III] emitting regions of ERQs are more compact. The Peto-Prentice test gives the probability that the ERQs and the comparison quasars follow the same distribution is only 0.03.

Based on Figs. 6 and 7 we conclude that the extremely fast ERQ-driven ionized outflows tend to be less extended than other AGN-driven ionized outflows controlled for luminosities and redshifts. As a low-density forbidden transition, [O III] 5007 cannot be produced on the scales of the broad-line region. The characteristic size of those spatially-unresolved [O III]-emitting regions has a physical lower limit at  $\sim 1$  kpc scales. Our results are consistent with the scenario that ERQs are in an earlier evolutionary stage than normal blue quasars and during this short-lived, transition blowout phase the outflows have not had enough time to further expand into their interstellar media. The difference between the extents of ERQ-driven outflows compared to those of Type II quasars suggests the physical conditions in ERQs are unique and beyond orientation differences as in the AGN unified model (Antonucci 1993; Netzer 2015). Our results are consistent with models of quasar feedback where IR radiation pressure trapped in dusty environments can boost powerful, galactic-scale outflows during their more compact and younger stages (Costa et al. 2018; Ishibashi et al. 2018). The post-starburst E+A galaxies, which are believed to be a transition stage from the active phase to the quenched phase of galaxy evolution, are found to have larger ionized outflow extents up to 17 kpc (Baron et al. 2018, 2024). Their outflow extents are also consistent with the supposed evolution sequence. While the extended dust in ERQ host galaxies can affect the

detectability of [O III] emission, we note that the broad [O III] component is compact even in ERQs where a narrow [O III] component is detected and extended.

#### 4.2 Small Total [O III]-Emitting Regions

Given that the ERQ-driven outflows tend to be compact, the extents of the PSF-subtracted residual [O III] emissions largely trace the extents of the quiescent ionized interstellar media. For the comparison sources, where the residual [O III] is spatially resolved we measure the maximum radius of a  $S/N > 2$  spaxel, and where the residual is unresolved we adopt a 0.5 arcsec upper limit. Fig. 8 presents the maximum radii of PSF-subtracted residual [O III] emissions versus bolometric luminosities of ERQs and other luminous quasars in the literature. The maximum radii of residual [O III] are formally presented as upper limits for many ERQs, as the adaptive-optics-corrected PSF still has a weak seeing halo. We refer to the half-light radii of the [O III] residuals in seven out of 10 ERQs. The fraction of ERQs with PSF-subtracted residuals present is similar to that of the luminous blue quasar sample of Kakkad et al. (2020) despite being suppressed by typically three magnitudes along the lines-of-sight in the rest-frame UV relative to the spectral energy distribution of normal quasars (Hamann et al. 2017). This suggests that some ionizing radiation is able to escape and the [O III] emission is not predominantly ionization-bounded, a conclusion that is also reached with comparing  $\text{Ly}\alpha$  haloes of ERQs and normal blue quasars (Lau et al. 2022; Gillette et al. 2023). On a related note, the fraction of ERQs having a narrow [O III] component, five out of 10, is also similar to the fraction of the Kakkad et al. (2020) luminous blue quasars having a narrow component.

Although PSF-subtracted residuals are present in ERQs, they tend to be less extended than in luminous blue quasars and the Type II quasar in comparison. The Pento-Prentice test gives the probability that the ERQs and the comparison quasars follow the same distribution is 0.11. This is consistent with ERQs having global and patchy obscuration patterns. The global obscuration explains the small extents of the total ionized emitting regions independently of the outflow timescales, while the patchiness still allows channels for ionizing radiation to escape. Such geometry of quasar obscuration has been explored in Andonie et al. (2024) with submillimeter data, which find that dusty starburst galaxies can contribute substantial galactic-scale obscuration comparable to the nuclear-scale obscuration level (see also Muñoz-Elgueta et al. 2022; González Lobos et al. 2023).

The ERQs J0006+1215, J1232+0912, J1652+1728, and J2323–0100 have their surrounding quasar-powered  $\text{Ly}\alpha$  haloes measured with wide-field integral-field spectroscopy (Lau et al. 2022; Gillette et al. 2023). We may combine analysis of their halo-scale  $\text{Ly}\alpha$  emissions and galactic-scale [O III] emissions to jointly assess the geometry of the quasar illumination. J0006+1215 has moderately suppressed  $\text{Ly}\alpha$  halo luminosity relative to luminous blue quasars or Type II quasars, whereas the total [O III]-emitting region has comparable extent as other quasar populations. J1232+0912 has moderately suppressed  $\text{Ly}\alpha$  halo luminosity, whereas the [O III]-emitting region has an unresolved size. J2323–0100 has heavily suppressed  $\text{Ly}\alpha$  halo luminosity, whereas the [O III]-emitting region is compact and resolvable only by the most excellent angular resolution and deep observations. J1652+1728 has a disturbed and luminous  $\text{Ly}\alpha$  halo, whereas the total [O III]-emitting region has comparable extent as other quasar populations. Overall, the halo-scale  $\text{Ly}\alpha$  measurements and galactic-scale [O III] measurements together present a picture that these ERQs are inconsistent with a simple Type II geometry.

Despite the aforementioned differences between ERQs and a sim-

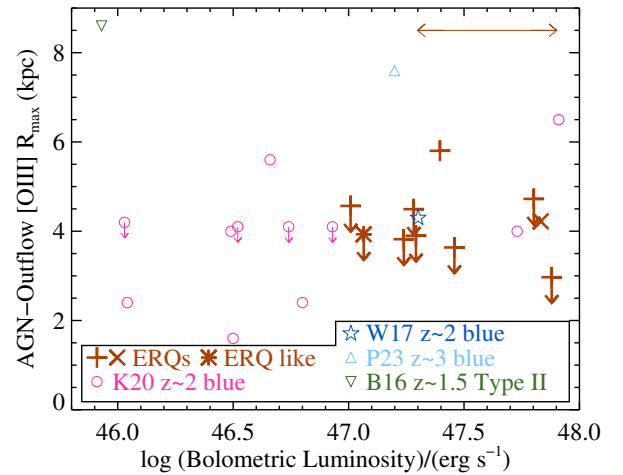


**Figure 6.** The maximum radii of AGN-driven [O III] outflows versus bolometric luminosities, of ERQs and other luminous quasars at cosmic noon in the literature. OSIRIS-measured ERQs are shown in brown plus symbols, the NIFS-measured ERQ from Vayner et al. (2021a) is shown in a brown cross symbol, and the red ERQ-like quasar is shown in a brown asterisk symbol. The typical uncertainty in the luminosities of the ERQs is indicated with a horizontal double arrow. Blue quasars at  $z \sim 2$  from the Kakkad et al. (2020) sample are shown in pink circles. One blue quasar at  $z \sim 2$  from Williams et al. (2017) is shown in a blue star. One blue quasar at  $z \sim 3$  from Perna et al. (2023) is shown in a light blue upward triangle. One Type II quasar at  $z \sim 1.5$  from Brusa et al. (2016) is shown in a green downward triangle.

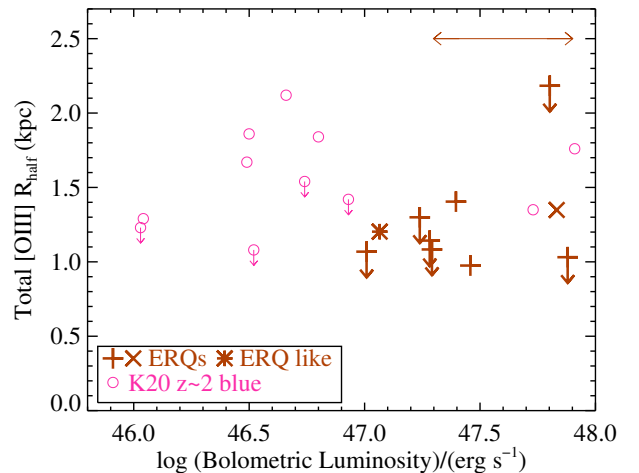


**Figure 7.** The half-light radii of total [O III] emissions versus bolometric luminosities, of ERQs and cosmic-noon luminous blue quasars from Kakkad et al. (2020). The symbol scheme follows Fig. 6.

ple Type II geometry, the hint of the presence of ionization cones in 4 out of 10 ERQs suggests some of the obscuration patterns can be partially explained by the standard torus-based unified model. The idea of a patchy obscuring torus has been explored in Obied et al. (2016) to explain observations of scattered light in Type II quasars.

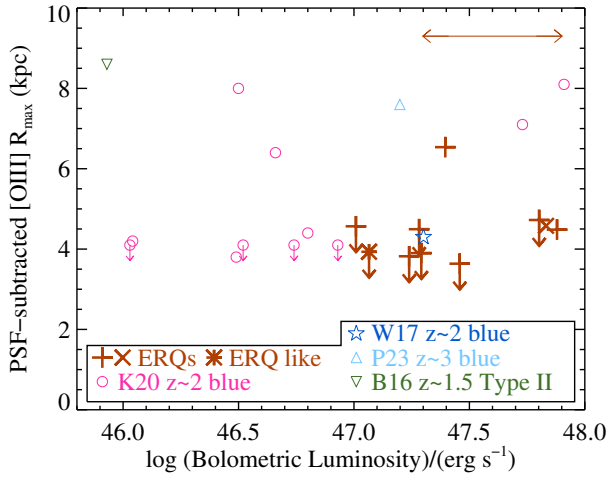


**Figure 8.** The maximum radii of PSF-subtracted residual [O III] emissions versus bolometric luminosities, of ERQs and other luminous quasars at cosmic noon in the literature. The symbol scheme follows Fig. 6.

## 5 CONCLUSIONS AND FUTURE WORK

ERQs are a non-radio-selected, intrinsically luminous population of quasars at cosmic noon redshifts selected by their extremely red colour from rest-frame UV to mid-IR. They are characterized by exceptionally broad and blueshifted [O III]  $\lambda\lambda 4959, 5007$  emission lines that carry outflow speeds reaching  $>6000 \text{ km s}^{-1}$ . We obtained new Keck/OSIRIS observations of nine ERQs and published Gemini/NIFS observations of one ERQ to form a sample of 10 ERQs with laser-guided adaptive-optics-assisted integral-field spectroscopy. The goal is to measure the sizes and spatially-resolved kinematics of the [O III]-emitting regions. We reached angular resolutions of  $\sim 0.2$  arcsec in Gaussian FWHM. We performed analysis on the [O III] and continuum emissions of the ERQs and their reference empirical PSFs, using the surface brightness radial profile method and the PSF subtraction method.

We identify extended, clumpy, disturbed continuum emission in the hosts of J0006+1215, J1217+0234, J1232+0912, and companion continuum emission around J2323–0100. We confirm signs of merger activities in ERQs although we do not quantify a merger fraction due to depth of the data.

For each ERQ we fit two to three Gaussian components to the [O III] emissions extracted from annular apertures, both before and after PSF subtraction. We consider a kinematic component to be tracing AGN-driven outflow if its velocity dispersion  $\geq 250 \text{ km s}^{-1}$ . For the overall sample, the 16 fitted [O III] components that exceed the AGN-outflow threshold are spatially unresolved or compact with maximum radii  $\leq 4 \text{ kpc}$ . There are five [O III] components of the sample below the AGN-outflow cut and all are extended, possibly tracing the quiescent interstellar media on few kpc scales. Justified on their different spatial distributions and bimodality in the components' velocity distribution, we consider the broad versus narrow components physical distinct and having different dynamical mechanisms.

Compared to other radio quiet, intrinsically luminous quasars at cosmic noon, the extremely fast ERQ-driven [O III] outflows appear to be compact, at  $\sim 1 \text{ kpc}$  scales. Fast and compact ionized outflows support the notion that ERQs are young quasars, representing a short-lived, transition, blowout phase in galaxy evolution, and their unique physical conditions cannot be explained by Type I versus Type II

orientation differences. Our results are consistent with models of quasar feedback where IR radiation trapped by dust produces faster and more compact outflows.

The fraction of total [O III] emission being spatially resolved in ERQs is similar to that in other luminous quasars, suggesting that some of the ionizing radiation has channels to escape through the dust obscuration. The total [O III]-emitting regions in ERQs, at few kpc scales, appear to be less extended compared to other luminous quasars. Resolved but small extents of the total [O III] emissions support ERQs having global and patchy obscuration patterns that are inconsistent with a simple Type II geometry. The hint of ionization cones in 4 out of 10 ERQs suggests some of the obscuration patterns can also be partially explained by a patchy torus model.

Finally, both the current generation of adaptive optics and JWST NIRSpec integral-field observations have PSF wings extending out to  $\sim 1$  arcsec (Law et al. 2018; Veilleux et al. 2023). How the ionized outflows traced by [O III] compare to the unobscured star formation traced by  $H\alpha$  in quasar-host galaxies remains an open question. Should there be evidence of suppression of star formation by quasar feedback manifested as spatial anticorrelation between [O III] and  $H\alpha$ , new-generation instruments such as the VLT/ERIS and the Keck I/Liger are needed to detect it.

## ACKNOWLEDGEMENTS

We acknowledge Gene C. K. Leung, Eilat Glikman, and Sanchit Sabhlok for discussions. We acknowledge Sherry Yeh, Jim Lyke, and Randy Campbell for supporting the observations. We acknowledge Devin Chu, Andrea Ghez, and Luke Finnerty for sharing their data. MWL, FH, and JG acknowledge support from the USA National Science Foundation grant AST-1911066. NLZ acknowledges support from NASA ADAP grant 80NSSC21K1569. This research was supported in part by the National Science Foundation under Grant No. NSF PHY-1748958. This work is based on observations made at the W. M. Keck Observatory, which is operated as a scientific partnership between the California Institute of Technology and the University of California. It was made possible by the generous support of the W. M. Keck Foundation. The authors wish to recognize and acknowledge the very significant cultural role and reverence that the summit of Mauna Kea has always had within the indigenous Hawaiian community. We are most fortunate to have the opportunity to conduct observations from this mountain.

## DATA AVAILABILITY

The data are available upon request.

## REFERENCES

- Andonie C., et al., 2024, *MNRAS*, **527**, L144
- Antonucci R., 1993, *ARA&A*, **31**, 473
- Assef R. J., et al., 2015, *ApJ*, **804**, 27
- Banerji M., Alaghband-Zadeh S., Hewett P. C., McMahon R. G., 2015, *MNRAS*, **447**, 3368
- Baron D., et al., 2018, *MNRAS*, **480**, 3993
- Baron D., Netzer H., Lutz D., Davies R. I., Prochaska J. X., 2024, *arXiv e-prints*, p. [arXiv:2401.09576](https://arxiv.org/abs/2401.09576)
- Barro G., et al., 2023, *arXiv e-prints*, p. [arXiv:2305.14418](https://arxiv.org/abs/2305.14418)
- Bischetti M., et al., 2017, *A&A*, **598**, A122
- Brusa M., et al., 2016, *A&A*, **588**, A58
- Calistro Rivera G., et al., 2021, *A&A*, **649**, A102

- Canalizo G., Stockton A., 2001, *ApJ*, **555**, 719
- Chen C.-C., et al., 2017, *ApJ*, **846**, 108
- Costa T., Rosdahl J., Sijacki D., Haehnelt M. G., 2018, *MNRAS*, **479**, 2079
- Costa T., Arrigoni Battaia F., Farina E. P., Keating L. C., Rosdahl J., Kimm T., 2022, *MNRAS*, **517**, 1767
- Cresci G., et al., 2015, *ApJ*, **799**, 82
- Cresci G., et al., 2023, *A&A*, **672**, A128
- Croton D. J., et al., 2006, *MNRAS*, **365**, 11
- Eisenstein D. J., et al., 2011, *AJ*, **142**, 72
- Feigelson E. D., Nelson P. I., Isobe T., LaValley M., 2014, ASURV: Astrophysical SURVival Statistics, Astrophysics Source Code Library, record ascl:1406.001 (ascl:1406.001)
- Finnerty L., et al., 2020, *ApJ*, **905**, 16
- Gebhardt K., et al., 2000, *ApJ*, **539**, L13
- Gillette J., Lau M. W., Hamann F., Perrotta S., Rupke D. S. N., Wylezalek D., Zakamska N. L., Vayner A., 2023, *MNRAS*, **526**, 2578
- Gillette J., Hamann F., Lau M. W., Perrotta S., 2024, *MNRAS*, **527**, 950
- Glikman E., et al., 2022, *ApJ*, **934**, 119
- González Lobos V., et al., 2023, *A&A*, **679**, A41
- Hamann F., et al., 2017, *MNRAS*, **464**, 3431
- Harrison C. M., et al., 2016, *MNRAS*, **456**, 1195
- Hopkins P. F., Elvis M., 2010, *MNRAS*, **401**, 7
- Hopkins P. F., Hernquist L., Cox T. J., Di Matteo T., Robertson B., Springel V., 2006, *ApJS*, **163**, 1
- Hopkins P. F., Hernquist L., Cox T. J., Kereš D., 2008, *ApJS*, **175**, 356
- Hopkins P. F., Torrey P., Faucher-Giguère C.-A., Quataert E., Murray N., 2016, *MNRAS*, **458**, 816
- Ishibashi W., Fabian A. C., Maiolino R., 2018, *MNRAS*, **476**, 512
- Kakkad D., et al., 2020, *A&A*, **642**, A147
- Kakkad D., et al., 2023, *MNRAS*, **520**, 5783
- Lau M. W., Hamann F., Gillette J., Perrotta S., Rupke D. S. N., Wylezalek D., Zakamska N. L., 2022, *MNRAS*, **515**, 1624
- Law D. R., Steidel C. C., Chen Y., Strom A. L., Rudie G. C., Trainor R. F., 2018, *ApJ*, **866**, 119
- Liu G., Zakamska N. L., Greene J. E., Nesvadba N. P. H., Liu X., 2013, *MNRAS*, **436**, 2576
- Lockhart K. E., et al., 2019, *AJ*, **157**, 75
- Lylke J., et al., 2017, OSIRIS Toolbox: OH-Suppressing InfraRed Imaging Spectrograph pipeline, Astrophysics Source Code Library, record ascl:1710.021 (ascl:1710.021)
- Monadi R., Bird S., 2022, *MNRAS*, **511**, 3501
- Muñoz-Elgueta N., Arrigoni Battaia F., Kauffmann G., De Breuck C., García-Vergara C., Zanella A., Farina E. P., Decarli R., 2022, *MNRAS*, **511**, 1462
- Nelson D., et al., 2019, *MNRAS*, **490**, 3234
- Nesvadba N. P. H., De Breuck C., Lehnert M. D., Best P. N., Collet C., 2017, *A&A*, **599**, A123
- Netzer H., 2015, *ARA&A*, **53**, 365
- Noboriguchi A., et al., 2019, *ApJ*, **876**, 132
- Noboriguchi A., Inoue A. K., Nagao T., Toba Y., Misawa T., 2023, *ApJ*, **959**, L14
- Obied G., Zakamska N. L., Wylezalek D., Liu G., 2016, *MNRAS*, **456**, 2861
- Perna M., et al., 2015, *A&A*, **583**, A72
- Perna M., et al., 2023, *A&A*, **679**, A89
- Perrotta S., Hamann F., Zakamska N. L., Alexandroff R. M., Rupke D., Wylezalek D., 2019, *MNRAS*, **488**, 4126
- Ross N. P., et al., 2015, *MNRAS*, **453**, 3932
- Rupke D. S. N., 2014, IFSRED: Data Reduction for Integral Field Spectrographs (ascl:1409.004)
- Sanders D. B., Soifer B. T., Elias J. H., Neugebauer G., Matthews K., 1988, *ApJ*, **328**, L35
- Shen Y., 2016, *ApJ*, **817**, 55
- Shen L., et al., 2023, *Science Advances*, **9**, eadg8287
- Soliman N. H., Hopkins P. F., 2023, *MNRAS*, **525**, 2668
- Sun A.-L., Greene J. E., Zakamska N. L., 2017, *ApJ*, **835**, 222
- Urrutia T., Lacy M., Becker R. H., 2008, *ApJ*, **674**, 80
- Vayner A., et al., 2021a, *MNRAS*, **504**, 4445
- Vayner A., et al., 2021b, *ApJ*, **919**, 122
- Vayner A., et al., 2023, *ApJ*, **955**, 92
- Vayner A., et al., 2024, *ApJ*, **960**, 126
- Veilleux S., et al., 2023, *ApJ*, **953**, 56
- Villforth C., 2023, *The Open Journal of Astrophysics*, **6**, 34
- Williams R. J., Maiolino R., Krongold Y., Carniani S., Cresci G., Mannucci F., Marconi A., 2017, *MNRAS*, **467**, 3399
- Wright E. L., 2006, *PASP*, **118**, 1711
- Wright E. L., et al., 2010, *AJ*, **140**, 1868
- Wylezalek D., et al., 2022, *ApJ*, **940**, L7
- Zakamska N. L., Greene J. E., 2014, *MNRAS*, **442**, 784
- Zakamska N. L., et al., 2016, *MNRAS*, **459**, 3144
- Zakamska N. L., et al., 2019, *MNRAS*, **489**, 497
- Zubovas K., King A., 2012, *ApJ*, **745**, L34

This paper has been typeset from a  $\text{\LaTeX}$  file prepared by the author.